

The CERES/NA45 Radial Drift Time Projection Chamber

D. Adamová^a, G. Agakichiev^b, D. Antończyk^b,
H. Appelshäuser^c, V. Belaga^d, J. Bielčíková^e,
P. Braun-Munzinger^b, R. Campagnolo^{f,h}, A. Cherlin^g,
S. Damjanović^h, T. Dietel^h, L. Dietrich^h, A. Dreesⁱ,
W. Dubitzky^h, S.I. Esumi^h, K. Filimonov^h, Z. Fraenkel^g,
C. Garabatos^b, P. Glässel^h, G. Hering^b, J. Holeczek^b,
V. Kushpil^a, A. Marín^b, J. Milošević^h, A. Milov^g,
D. Miśkowiec^b, L. Musa^f, Y. Panebrattsev^d, O. Pechenova^d,
V. Petráček^h, A. Pfeiffer^f, J. Rak^e, I. Ravinovich^g,
M. Richter^h, H. Sako^b, E. Schäfer^h, W. Schmitz^h,
J. Schukraft^f, W. Seipp^h, A. Sharma^f, S. Shimansky^d,
J. Stachel^h, M. Šumbera^a, H. Tilsner^h, I. Tserruya^g,
J. P. Wessels^j, T. Wienold^h, B. Windelband^h, J. P. Wurm^e,
W. Xie^g, S. Yurevich^h, V. Yurevich^d

^a*NPI/ASCR, Řež, Czech Republic*

^b*Gesellschaft für Schwerionenforschung, Darmstadt, Germany*

^c*University Frankfurt, Germany*

^d*Joint Institute for Nuclear Research, Dubna, Russia*

^e*Max-Planck-Institut für Kernphysik, Heidelberg, Germany*

^f*CERN, Geneva, Switzerland*

^g*Weizmann Institute, Rehovot, Israel*

^h*University Heidelberg, Germany*

ⁱ*Department of Physics and Astronomy, SUNY Stony Brook, USA*

^j*University Münster, Germany*

Abstract

The design, calibration, and performance of the first radial drift Time Projection Chamber (TPC) are presented. The TPC was built and installed at the CERES/NA45 experiment at the CERN SPS in the late nineties, with the objective to improve the momentum resolution of the spectrometer. The upgraded experiment took data twice, in 1999 and in 2000. After a detailed study of residual distortions a spatial resolution of $340\text{ }\mu\text{m}$ in the azimuthal and $640\text{ }\mu\text{m}$ in the radial direction was achieved, corresponding to a momentum resolution of $\Delta p/p = \sqrt{(1\% \cdot p/\text{GeV})^2 + (2\%)^2}$.

Key words: radial drift TPC, field cage, pad plane, gating grid, readout electronics, pad response, cooling system, gas composition, drift velocity, calibration, alignment, field calculation, pattern recognition, tracking
PACS: 29.40.Gx

1 Introduction

Heavy-ion collisions at ultra-relativistic energies offer the possibility to study the behavior of nuclear matter at high density and/or temperature where one expects the formation of the Quark Gluon Plasma (QGP). A valuable tool to explore the early stage of heavy-ion collisions are electromagnetic probes. They are not subject to the strong interaction and can freely escape the surrounding hadronic medium.

CERES/NA45 (Cherenkov Ring Electron Spectrometer) is the only experiment at the CERN Super Proton Synchrotron (SPS) dedicated to the study of e^+e^- -pairs produced in p-A and A-A collisions in the low mass range of $0.1\text{ GeV}/c^2 < m_{ee} < 1.2\text{ GeV}/c^2$. It was installed in 1990 at the H8 beam line of the SPS North Area and started its operation in 1991. Systematic studies have been done using S-Au interactions in 1992 and proton-induced reactions p-Be and p-Au in 1993. An energy scan of Pb-Au interactions has been performed in beam times from 1995 to 2000. One of the main achievements of the CERES experiment is the measurement of an enhanced dilepton yield in S-Au and Pb-Au collisions as compared to expected contributions from vacuum decays of hadrons [1,2,3,4,5].

In 1998 the experiment was upgraded with a radial drift Time Projection Chamber (TPC) [6,7] in order to significantly improve the mass resolution in the range of the ϕ -meson from $\Delta m/m = 7\%$ [5] to 3.8% [8,9]. The additional information from the differential energy loss dE/dx in the TPC further improved the pion/electron separation capability. At an electron efficiency of 0.68 the pion misidentification rate dropped from $5 \cdot 10^{-4}$ to $2.5 \cdot 10^{-5}$ at a particle momentum of $1\text{ GeV}/c$ [10,11]. The dilepton invariant mass spectra measured after the experimental upgrade with the TPC allowed for the first

time to discriminate between different theoretical approaches [10,12]. Finally, the TPC also opened the possibility to study hadronic channels. Since then many interesting topics have been addressed like particle multiplicities, elliptic flow, event-by-event fluctuations, particle correlations, and strangeness analyses (see for example [9]).

The upgraded CERES spectrometer, as it was used during the heavy-ion runs in 1999 and 2000, is shown in Fig. 1. The main components of the experiment are two Silicon Drift Detectors (SDD1, SDD2) for vertex reconstruction, two Ring Imaging Cherenkov Counters (RICH1, RICH2) for electron identification, and a radial drift Time Projection Chamber (TPC) for the measurement of the particle momentum and particle identification. All detector components of the spectrometer cover full azimuth at polar angles $8^\circ < \theta < 14^\circ$, corresponding to a pseudorapidity range of $2.10 < \eta < 2.65$.

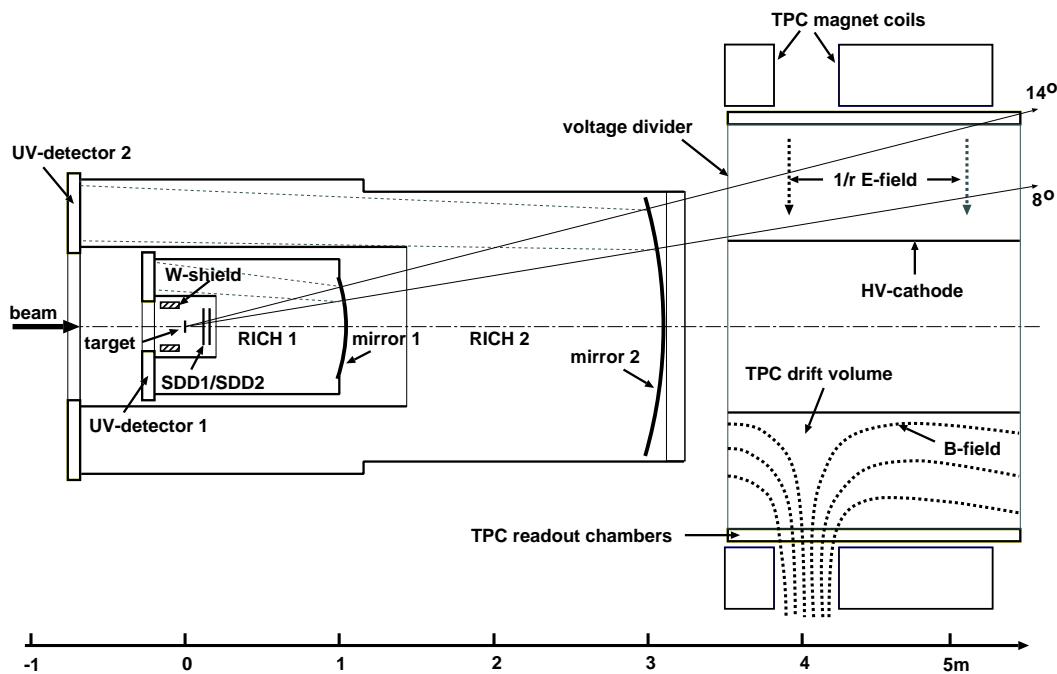


Fig. 1. Schematic view of the CERES/NA45 spectrometer. The TPC is operated inside an inhomogeneous magnetic field generated by two opposite polarity coils. The electric field inside the TPC is radial, pointing from the readout chambers to the high voltage cylinder.

2 TPC design considerations

The aim of an improved mass resolution required the addition of a charged particle spectrometer to the existing CERES experiment, consisting of a magnet system and a large volume electron tracking device [13,14]. The TPC technology has been successfully applied for this task in heavy-ion experiments,

combining high resolution tracking with large acceptance, low material budget, and reasonable cost.

The new spectrometer system had to preserve the polar angle acceptance and the azimuthal symmetry of the existing experiment. This led to a radial electric field configuration resulting in the first radial drift TPC ever to be operated. In addition, a magnetic field configuration with two new magnet coils around the TPC has been adopted providing a strong radial component for momentum determination (cf. Fig. 1 and Sect. 5). With a momentum dependent curvature in the r - ϕ plane the ionization electrons drift almost radially outwards to the readout chambers which are installed on the outer circumference of the TPC.

For significant parts of the drift volume this design implies crossing electric and magnetic field lines leading to a finite variable Lorentz angle of the drifting electrons. The drift gas mixture Ne/CO₂ (80%/20%) has been found as an optimum with regard to small diffusion coefficients and Lorentz angle, sufficient primary ionization, long radiation length, and detector stability. In addition, the maximum drift time should be kept low in order not to compromise the trigger rate without requiring excessively high drift fields.

3 Mechanical layout

The TPC was installed downstream of the existing spectrometer, at a distance of 3.8 m from the target system. A cross-section of the TPC is shown in Fig. 2. The mechanical stability of the TPC is provided by a massive backplate and an outer cylinder, both in aluminum. The active volume of about 9 m³ is filled with a gas mixture of Ne/CO₂ (80%/20%). It is enclosed by the inner high voltage cylinder at $r = 486$ mm, the 16 readout chambers at $r \approx 1.3$ m, and two 50 μ m Kapton^{®1} foils with thin Cu voltage dividers at the front and the end faces. The active length of the TPC is 2 m. The ionization electrons created along charged particle tracks drift outwards and are detected in the readout chambers, Multi Wire Proportional Chambers (MWPC) with cathode pad-readout. The TPC is operated in a magnetic field which predominantly deflects charged particles in azimuth, and provides the reconstruction of up to 20 space points along the particle track.

4 Electric field

The electric drift field follows a $1/r$ -dependence varying between 600 and 200 V/cm (Fig. 3). In Ne/CO₂ (80%/20%) this corresponds to non-uniform drift velocities between 0.7 and 2.4 cm/ μ s and a maximum drift time of 71 μ s.

¹ Kapton[®] is a registered trademark of E. I. du Pont de Nemours and Company

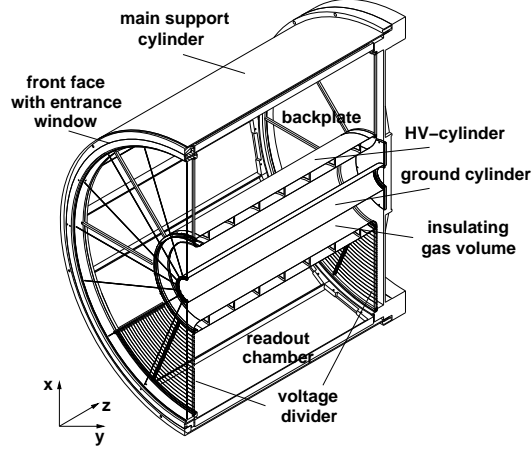


Fig. 2. Cross-section of the CERES TPC. The front and end faces are closed with Kapton[®] foils which, together with the inner high voltage cylinder and the readout chambers, form a field cage and enclose the drift volume filled with Ne/CO₂. An insulating gap between the two inner cylinders of 8 cm width is flushed with CO₂.

The electric field has a small azimuthal component due to the polygonal outer shape of the TPC and a small longitudinal component at the end caps.

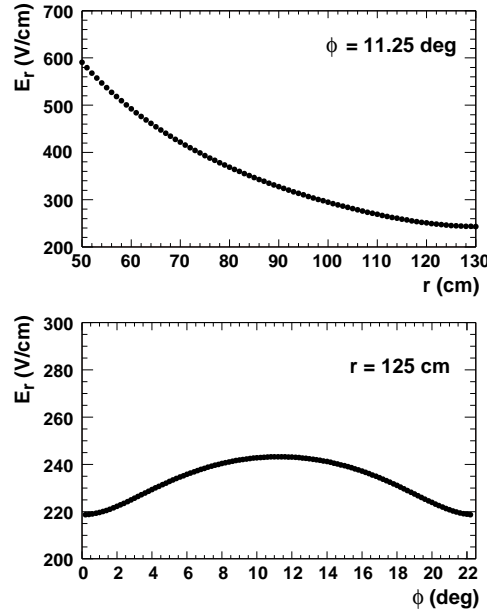


Fig. 3. Radial component of the electric field vector as a function of the radius r and the azimuthal coordinate ϕ (1 readout chamber $\equiv 22.5^\circ$).

4.1 Field cage

The field cage foils of the TPC are supposed to match the radial drift field at the ends of the drift volume and to provide gas tightness. This must be achieved at a minimum of material budget and with a mechanically and electrostatically stable structure.

The foils are made of $50\,\mu\text{m}$ thick Kapton[®] coated on both sides with 42 copper concentric circular strips. The copper strips have a thickness of $200\,\mu\text{m}$. They are 15 mm wide and 5.46 mm apart from each other. The foils are composed of four pieces covering 90 degrees and are supported by 8 stesalit bars of 1 cm width and thickness. The bars are wrapped in Kapton[®] foil with the same copper pattern. In this case the copper layer is $4\,\mu\text{m}$ thick. The bars are connected to an inner and an outer Al ring which are attached to the HV-cylinder and the outer structure ('hamster cage'), respectively. The metal of the two sides of each foil is connected at the edges via small folded copper sheets of 0.5 mm thickness soldered to each strip. The copper sheets are used to solder the foils to the supporting bars. The intermediate bars are connected to the field cage with silver conducting epoxy. For mechanical stability and gas tightness, epoxy (Araldit 106) is applied along all the bars.

The electric diagram of the voltage divider is shown in Fig. 4. A voltage of $-29.2\,\text{kV}$ is applied to the inner cylinder via a $0.5\,\text{M}\Omega$ resistor. Two resistor chains are connected to the cylinder on one side and to the ground on the other. The resistors are regular carbon film resistors. They are soldered onto the strips of one bar. Because the matching field is radial and the strip pitch is constant, the resistor values must follow a $1/r$ -dependence. The resistor values range from $16\,\text{M}\Omega$ to $4\,\text{M}\Omega$. The total current in each chain is $80\,\mu\text{A}$. The currents are measured via the voltage drop on the external $9.95\,\text{k}\Omega$ test resistors in series with the chains. The bars and the resistors are inside the drift volume.

The resistors in the voltage dividers were chosen such that the strips should ensure a longitudinally homogeneous electric field inside the drift volume. However, it turned out that the resistance of some of the resistors used in the voltage dividers changed with the applied voltage. This resulted in a distortion of the drift field near the ends of the TPC which produced deviations of up to 4 cm, as observed with laser tracks. A three dimensional calculation of the electric field with detailed geometry and appropriately adjusted resistor values accounted for this effect and reduced the track distortions by a factor of 6.

4.2 Field calculation

The electric field calculation was performed using a custom program based on the relaxation method, including the proper knowledge of the ring potentials (Sect. 4.1) and the leakage of the amplification field through the cathode wire plane of the readout chambers (Sect. 7.1). An example of the potential

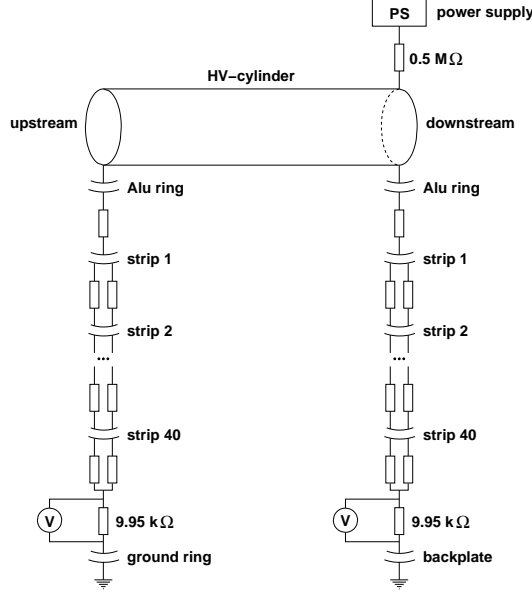


Fig. 4. Electric scheme of the field cage. A high voltage of 29.2 kV is applied to the inner cylinder. Two resistor chains supply potentials to the upstream and downstream rings. The two field cage currents are monitored via the voltage drop on the 9.95 kΩ test resistors.

calculated in the vicinity of the upstream field cage rings is shown in Fig. 5. The calculation was performed for half of a chamber (corresponding to 11.25°) assuming chamber symmetry. The code heavily exploited the symmetries of the detector and thus allowed to calculate a potential map within several hours running time on a personal computer. This would be impossible using a standard field computation tool like [15]. Indeed, the drift field obtained by running this package for 6 days was still exhibiting non-physical inhomogeneities on the level of several percent.

4.3 Corrections at the ends of the TPC

After accounting for the variation of the field cage resistors with the voltage the deviations of the reconstructed laser tracks from a straight line went down from 4 cm to 5–7 mm. The final tuning was done by adding a phenomenological correction potential calculated requiring $V = 0$ at the inner cylinder and the readout chambers, with the shape optimized to straighten the laser tracks (Fig. 6).

4.4 Correction for misalignment

The three-dimensional field calculation, needed to account at the same time for the polygonal readout chamber configuration ($r(\phi) \neq \text{const}$) and for the track curvature in $r(z)$, was done for performance reasons only for a 11.25° slice in ϕ of the TPC, i.e. for half a readout chamber. The azimuthal symme-

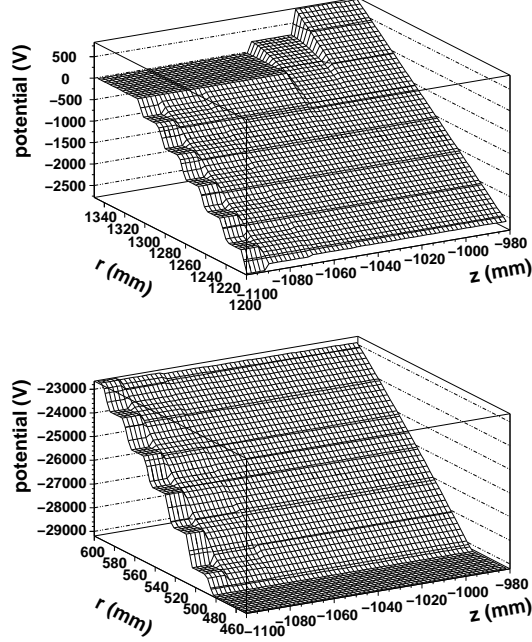


Fig. 5. Electric potential $V(r, z)$ in the vicinity of the upstream end of the TPC close to the outer cylinder (top) and close to the inner cylinder (bottom). Both calculations were performed at an azimuthal angle corresponding to the center of a chamber. The steps are caused by the field cage rings. The calculation grid is $(dr, d\phi, dz) = (1 \text{ mm}, 0.25^\circ, 2 \text{ cm})$. The sensitive volume is within $-1000 \text{ mm} < z < 1000 \text{ mm}$.

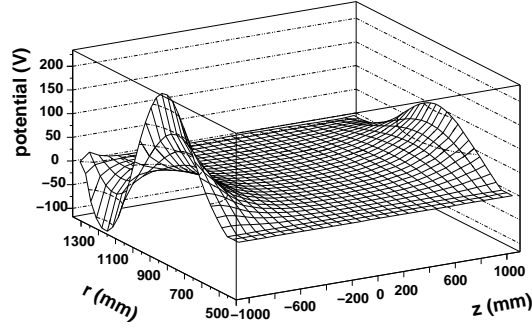


Fig. 6. The residual correction potential map needed to straighten the reconstructed laser tracks. The correction is larger at the upstream end of the TPC.

try, however, is broken by slight misalignments of the 16 chambers. To account for this, a number of two-dimensional potential calculations $V(r, \phi)$ was performed for a complete set of 16 chambers (Fig. 7), and then repeated with one of the chambers being slightly displaced in r or tilted in r vs. ϕ (Fig. 8). The correction potentials, defined as the difference between a two-dimensional calculation for a displaced (or tilted) and a perfectly aligned chamber

$$V_{cor}(r, \phi) = V_{misaligned}(r, \phi) - V_{ideal}(r, \phi) \quad (1)$$

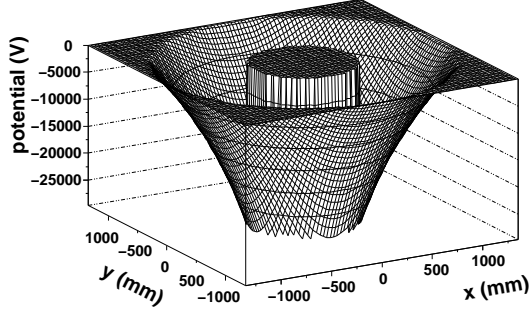


Fig. 7. Two-dimensional electric potential $V(r, \phi)$ calculated with all chambers at their nominal positions.

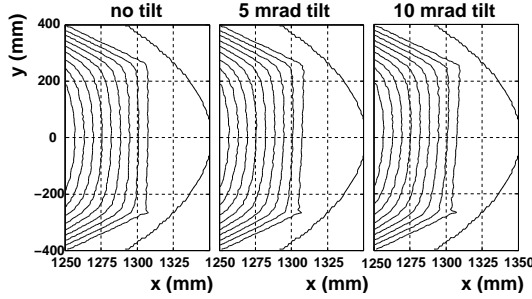


Fig. 8. Equipotential lines calculated with the chamber at its nominal position (left) and with two values of tilt (middle and right). Correction maps, defined as the difference between a displaced map and a nominal one, were added to the three-dimensional potential calculated with the ideal geometry.

were then added to the three-dimensional calculations, separately for each chamber and each of the 20 z -planes. The displacements in r and the tilts in $r(\phi)$ were chosen such as to move the reconstructed position of the high voltage cylinder as close as possible to the nominal $r = 486$ mm (maximum measured deviation of 0.3 mm). The high voltage cylinder is visible in the data either via the electrons knocked out from aluminum by the laser light or as the edge in the radial distribution of hits in physics events. One should note that displacing a chamber affects the reconstructed cylinder position in two ways: via the modified field and via the change in the path length. Both mechanisms were studied separately and in combination. Displacing a chamber by 1 mm without changing the field shifts the reconstructed cylinder by 3 mm (this is because the drift velocity close to the cylinder is three times higher than at the chamber). Using a field calculated with a chamber displaced by 1 mm but keeping the path length unchanged also gives a 3 mm shift. The combination of the two (as expected in a real case) gives a 4–5 mm apparent shift.

Displacements and tilts by up to 1.2 mm and 6 mrad, respectively, are needed to get the reconstructed cylinder to its nominal position and shape. Figs. 9 and 10 show the HV-cylinder position reconstructed before and after applying this correction, respectively. The data in the figures have been corrected for the pad-to-pad trace length variations (Sect. 8.5).

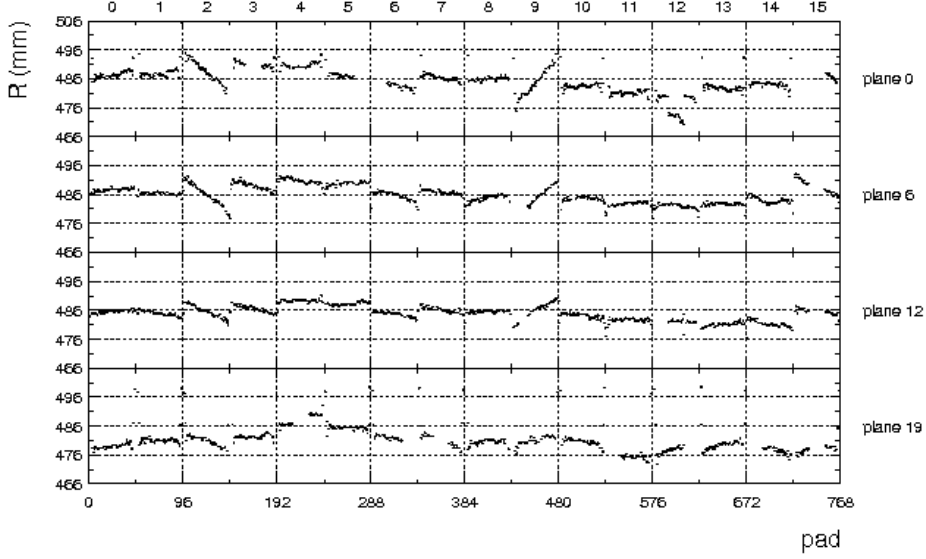


Fig. 9. Reconstructed edge of the radial distribution of hits before correcting for chamber positions. The data have been corrected for the pad-to-pad trace length variations.

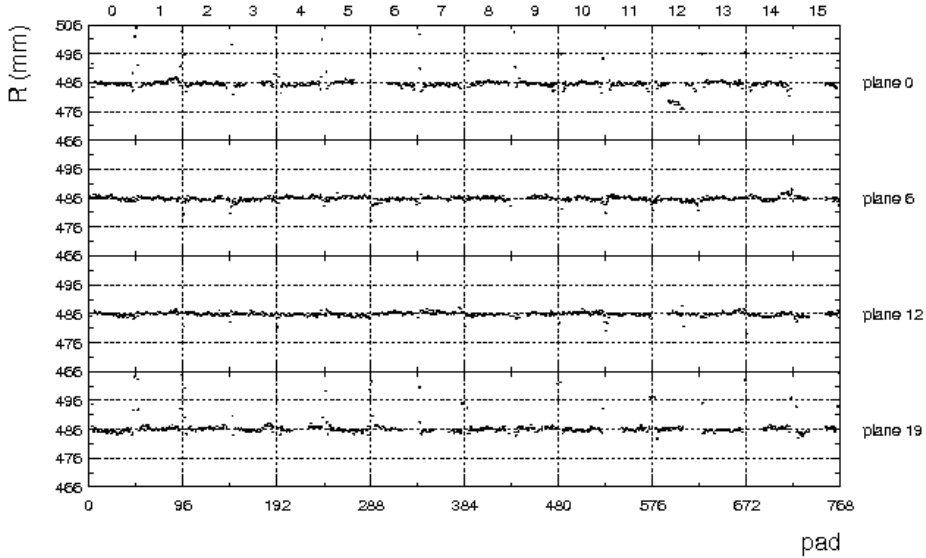


Fig. 10. Reconstructed edge of the radial distribution of hits after correcting for chamber positions. The data have been corrected for the pad-to-pad trace length variations.

5 Magnetic field

The TPC is operated inside an inhomogeneous magnetic field generated by two solenoidal coils with opposite sense currents of up to 4 kA. Fig. 11 shows a calculation of the magnetic field using the CERN POISSON package [16]. In the region between the two coils a field strength of 0.5 T is reached. Particles are deflected primarily in azimuthal direction. The field integral is

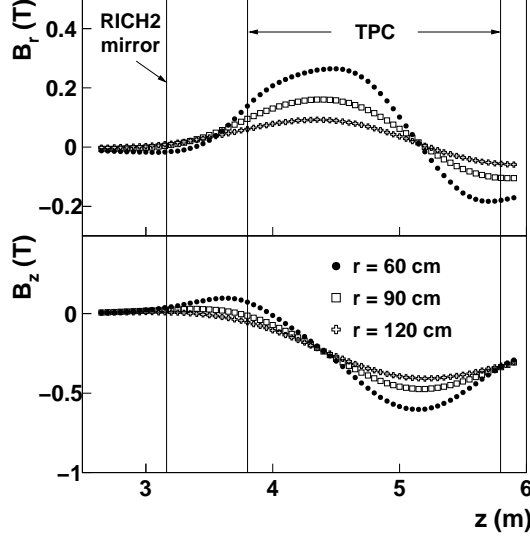


Fig. 11. Radial and longitudinal component of the magnetic field as a function of the longitudinal coordinate z for different radii r . The active region of the TPC and the position of the mirror of the RICH2 detector are indicated by vertical lines.

0.18 Tm at $\theta = 8^\circ$ and 0.38 Tm at $\theta = 14^\circ$. The magnetic fringe field outside the TPC drops off rapidly and is negligible at the position of the mirror of the RICH2 detector of the CERES spectrometer. The magnetic field was mapped (in presence of all TPC support structures) prior to installation of the TPC in the experimental area. The measurements correspond to the calculations with deviations from azimuthal symmetry at the percent level. These deviations are included in the analysis as corrections to the nominal field map [10].

6 Counting gas

The commonly used Ar/CH₄ (90%/10%) mixture was excluded as counting gas for its large Lorentz angles ($60^\circ - 70^\circ$ in the relevant field range), diffusion coefficients, and multiple scattering angle. In good approximation, the width of the angular distribution caused by multiple scattering is given by [17,18]

$$\theta_{ms} = \frac{13.6 \text{ MeV}}{\beta c p} Z \sqrt{\frac{x}{X_0}} \left(1 + 0.038 \ln \frac{x}{X_0} \right), \quad (2)$$

where p is the momentum in MeV/ c , βc is the velocity, Z is the charge number of the traversing particle, and x/X_0 is the thickness of the medium in units of its radiation length. Thus, a counting gas with large radiation length minimizes the influence of multiple scattering. In terms of multiple scattering, Ne-based gas mixtures are preferable to Ar-based mixtures.

6.1 Drift velocity

The drift velocity of the ionization electrons in the gas as derived from the Langevin equation can be written as a function of the electric field \vec{E} and the magnetic field \vec{B} :

$$\vec{v}_d = \frac{\mu}{1 + (\omega\tau)^2} \left(\vec{E} + \omega\tau \frac{\vec{E} \times \vec{B}}{B} + (\omega\tau)^2 \frac{(\vec{E} \cdot \vec{B})\vec{B}}{B^2} \right). \quad (3)$$

In this equation τ is the mean time between two collisions. The cyclotron frequency ω is given by:

$$\omega\tau = \frac{e}{m} B\tau = B\mu \quad (4)$$

where μ is the electron mobility. The mobility is a function of the electric field, gas composition, pressure, and temperature.

6.2 Composition

The outlined considerations were the baseline for detailed simulations with the package MAGBOLTZ [19]. For a large number of gas mixtures the drift velocity, Lorentz angle, longitudinal, and transverse diffusion coefficients were calculated as a function of the electric field for a given magnetic field at a fixed angle. The calculations cover magnetic fields from 0 T to 0.5 T at angles between 0° and 90° with respect to the electric field. Fig. 12 shows results for various gas mixtures for the most disadvantageous case of a magnetic field of 0.5 T perpendicular to the electric field [14]. The gas mixtures under considerations are Ne, He and Ar/He with admixtures of 10% to 20% CO₂. Also shown at the bottom of Fig. 12 are the diffusion coefficients normalized to the square root of the number of primary electrons n_e , since this ratio is the relevant quantity for the position resolution at the readout chamber.

Another limiting factor is the rate of clean interaction at a beam rate of $5 \cdot 10^5/\text{s}$ ($2 \cdot 10^6/\text{burst}$). This means that no further interaction should occur within a time window of twice the maximum drift time. A maximum drift time of $34 \mu\text{s}$ makes Ne/CO₂ (90%/10%) the preferred solution. He/Ar/CO₂ (45%/45%/10%) has the advantage of lower cost and yields, in terms of resolution, very similar performance but has a maximum drift time of $70 \mu\text{s}$. The final choice of 80% Ne and 20% CO₂ is a compromise between an optimum resolution and an acceptable loss of primary electrons, both of which are increasing with the fraction of CO₂. The latter is caused by the attachment of free electrons to oxygen impurities in the counting gas, with subsequent deexcitation through collisions with CO₂ molecules (Sect. 6.7). In addition, a higher concentration of quencher allows for a safer operation against glow discharges of Ne-based gas mixtures at relatively high gains. On the other hand,

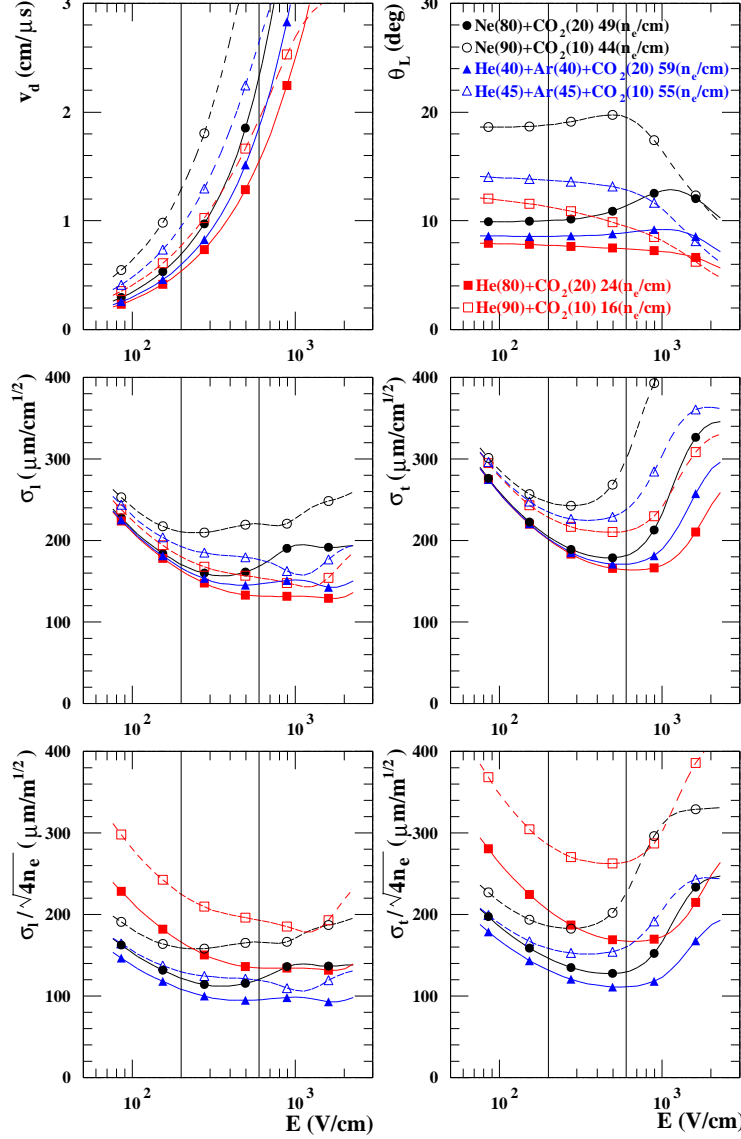


Fig. 12. MAGBOLTZ simulations for a magnetic field of 0.5 T perpendicular to the electric field. The drift velocity (top left), Lorentz angle (top right), longitudinal (middle left), and transverse (middle right) diffusion coefficients and the diffusion coefficients normalized to the square root of the number of primary electrons (bottom) were calculated for various gas mixtures. The vertical lines indicate the relevant range of the electric field in the CERES TPC.

CO₂-based mixtures are very sensitive to temperature and pressure fluctuations.

6.3 Gas system

In order to minimize the overall Ne consumption the gas system for the CERES TPC was designed as a closed loop circuit. The schematic is shown in

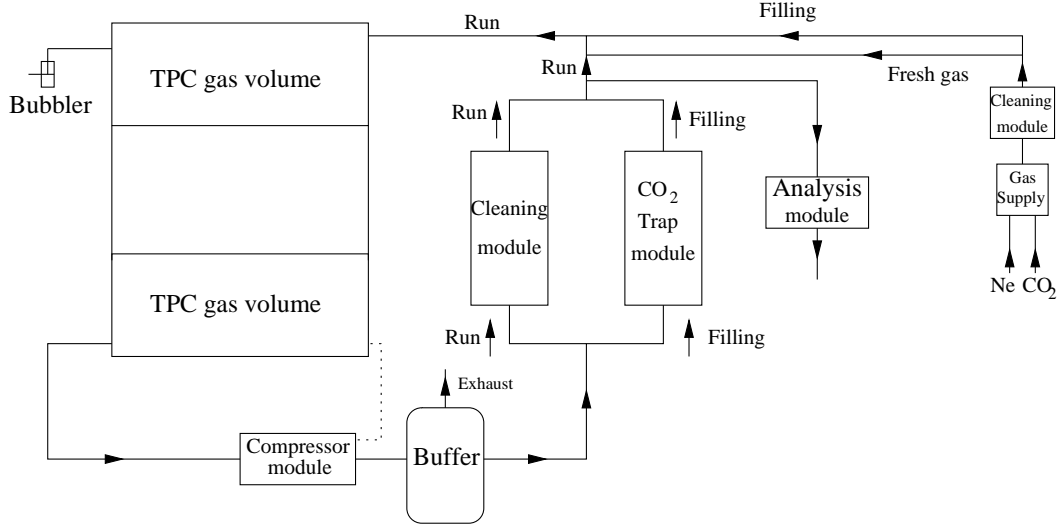


Fig. 13. Layout of the gas supply system of the CERES TPC. The copper catalyzers (cleaning module) remove oxygen and water vapor from the gas. The molecular sieves (trap module) trap CO_2 to bring the TPC to the correct gas mixture of Ne/ CO_2 (80%/20%).

Fig. 13. The majority of the gas mixture recirculates through the gas system cleaning part and the TPC. During a normal run small amounts of fresh gas ($0.12 \text{ m}^3/\text{h}$) are replaced. The gas circulation rate is about $1.4 \text{ m}^3/\text{h}$, corresponding to about 15% volume exchange per hour.

The gas system contains two compressors with a capacity of $3.7 \text{ m}^3/\text{h}$ each, located at the exit of the TPC. The recirculating gas flows through a buffer vessel and subsequently through one of two cartridges, filled with a copper catalyzer, to remove oxygen and water vapor. The purity and composition of the gas is monitored using oxygen, water, and CO_2 analyzers. Ambient pressure fluctuations are compensated for by filling or emptying gas from the buffer vessel, thus keeping a constant overpressure in the TPC. The pressure in the TPC is regulated at about 1 mbar above the atmospheric pressure. The operation of the system is controlled by a Programmable Logic Controller (PLC). A safety bubbler is installed at the detector to prevent any under- or overpressure at the TPC higher than 2 mbar, in particular during power failures.

The gas system can be operated either in an open system configuration for purging with CO_2 or in a special mode foreseen to bring the TPC to the correct mixture of Ne/ CO_2 filling. The latter is achieved with two parallel cartridges containing 2.7 kg of molecular sieve 13X each to absorb CO_2 . The cartridges are equipped with heating and cooling devices. A pump is connected to the output of the cartridges to vent the absorbed CO_2 . During the filling process the gas of the TPC is passed through one of the cartridges and the CO_2 is trapped. At the same rate Ne gas is injected into the system. Since Ne is not trapped the amount of Ne in the mixture increases with time. Once

the cartridge is saturated with CO_2 , the system changes automatically to the second cartridge and the first one is regenerated. Regeneration is achieved by heating the cartridge to 220°C while purging it with Ar and pumping the liberated CO_2 out of the system. After 1 hour the cooling line brings the cartridge to ambient temperature and the system switches over to the other cartridge. In this manner, no Ne is wasted while filling the detector. A total of 24 passes is necessary to trap 7.2 m^3 of CO_2 . The filling process takes about 50 hours.

6.4 Cooling system

The TPC requires a stable operating temperature which was set to 24°C . The sources of temperature variation are the proximity to the RICH detectors which are kept at 50°C , the magnet, the TPC readout electronics, and the hall environment. Three types of cooling circuits were installed: an insulating screen between the magnet and the TPC, cold screens against the heat from electronic cards, and CO_2 circuits.

- **Insulating screen.** The screen consists of two circuits of copper pipes with water circulating through them. The pipes are attached to the TPC's external aluminum cylinder by heat-transfer cement. Each circuit is connected to a temperature adjustable assembly to guarantee a constant temperature outside the TPC.
- **Cold screens.** Copper plates with a welded-on pipe are attached to each electronics card. The plates are water-cooled. The temperature is maintained above the dew point and it is the same on all the plates.
- **CO_2 insulating volumes.** Two closed CO_2 circuits, one in the TPC entrance window and one in the backplate, each 10 cm thick, are used to stabilize the temperature inside the TPC from variations in the hall, and/or RICH.

The water circuits are supplied via a Leakless Cooling System Version 2 (LCS2) [20], where the pressure is kept below atmospheric pressure. All the circuits are remotely controlled by a PLC. Individual PID controllers adjust the temperatures.

With this cooling system the short-term temperature variations could be stabilized to below 0.3°C during data taking periods.

6.5 Slow control

A computer driven system monitors all the parameters that could have an influence on the response of the TPC during the beam time (Fig. 14). These parameters include pressure, temperature, composition, oxygen and water content of the drift gas, drift velocity of electrons in the TPC, and the stability of the electric drift field. The gas monitoring system consists

of a personal computer (PC) running LINUX, a 16 channel 330 kHz 12-bit Analog-to-Digital-Converter (ADC) with programmable gain installed in the PC, a 192-bit Digital-Input-Output board (DIO), and a 48 channel Form C, 6 A relay.

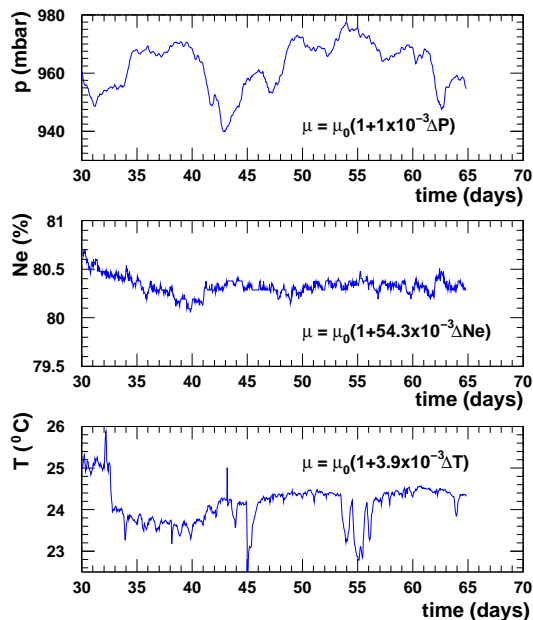


Fig. 14. The monitoring system of the CERES experiment surveyed all parameters that could influence the detector response, e.g. the pressure (top), gas composition (middle), and temperature (bottom). The changes of the nominal mobility μ due to these fluctuations are in the percent range.

The devices measuring the pressure, gas mixture and water content provide a voltage level which is read directly by the ADC. The TPC is equipped with three 16-bit PT100 temperature sensors. They are supplied with a constant current from an ISO-5B32 current input module. The reading is done sequentially using the relay which is driven by the DIO module. The oxygen level is recorded via a Orbisphere sensor with voltage level output. The drift velocity measurement is provided by a drift velocity monitor, known as GOOFIE [21], which is operated with the TPC gas mixture. The drift velocity monitor is read out with a LeCroy CAMAC Waveform Recorder 6810 and sent to a dedicated PC running WINDOWS. Via SAMBA the data are redirected to the LINUX PC, where they are stored and analyzed. The electric field stability is monitored by recording the high voltage, the total current through the voltage divider, and the voltage drop through two external resistors of the field cage.

6.6 Calibration of the drift velocity

Since the drift velocity in first order scales with the electric field, it is convenient to consider the ratio of the two, called electron mobility, in the absence of a magnetic field. The knowledge of the mobility for different values of the

electric field is essential for understanding drift in a radial field. Seven approximately parallel laser rays in one sector of the TPC, together with the signal from the HV-cylinder (photoelectric effect in the Al), were used to determine the electron mobility function. This was achieved by minimizing radial distances of the reconstructed TPC hits from the expected track positions. The expected track positions were calculated from the laser beam position before entering the TPC, measured with position sensitive diodes, and the known mirror positions and angles (cf. Sect. 9). In the case of the cylinder signal the reconstructed radius was compared to the nominal 486 mm. The 12 fit parameters included three factors for electric field corrections at each TPC end (Sect. 4.3), five parameters of the electron mobility curve, and the electronics time offset.

The five-parameter mobility curve obtained from the fit is shown as a dashed line with full dots in Fig. 15. The five parameters are the mobility values at $E = 10, 25, 35, 45$, and 65 V/mm, covering the range of electric field values at different positions in the TPC (cf. Fig. 3). The rest of the curve is an interpolation [22] between these points. This technique couples the parameters to specific drift regions and thus helps the fit to converge quickly. The measured mobility is compared to various versions of the simulation package MAGBOLTZ [19] in which the mobility is calculated microscopically based on the energy dependent cross sections for collisions of electrons on atoms and molecules. The deviation is significant and cannot be removed by even significant changes in the input gas composition or temperature (solid, dashed, dotted and dash-dotted lines).

6.7 *Electron attachment*

The noble gas neon in the TPC has an admixture of 20% carbon dioxide as quencher. The CO_2 improves the drift properties (cold gas) and prevents multiple discharges. It absorbs the photons emitted by excited atoms or deexcites the atoms directly through collisions. The energy mainly goes into rotational and vibrational excited molecular states and into ionization of the quencher.

However, the CO_2 molecules also interact with gas impurities like oxygen. Oxygen has the undesired property of attaching free electrons from primary ionization processes:



In dilute media the oxygen loses its energy by the reemission of the electron or by radiation. Unfortunately, at atmospheric pressure, as present in the TPC, the dominating process is the interaction with another molecule M:



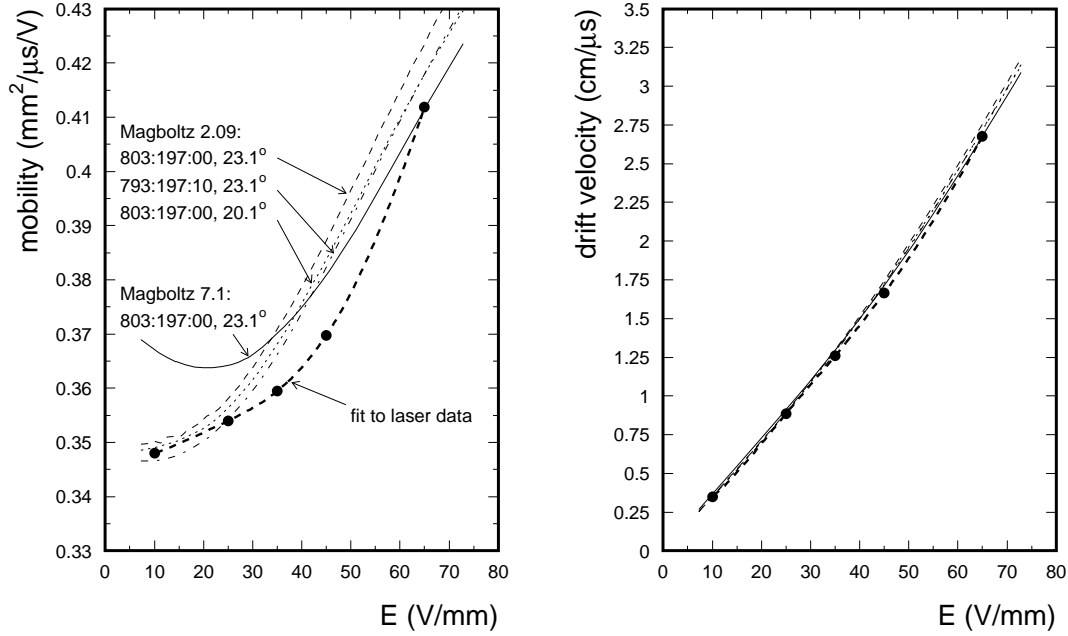
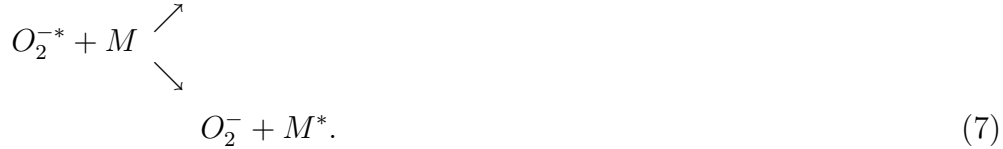


Fig. 15. Left: Mobility obtained from the fit to the laser data (dashed line with full dots). For comparison, the dashed, the dotted, and the dash-dotted lines show mobility calculations with MAGBOLTZ 2.09 for three gas compositions (Ne:CO₂:N₂) and temperature cases at a pressure of 971.5 mbar. The solid line shows an analogous calculation done with MAGBOLTZ 7.1. The difference between different versions of MAGBOLTZ originate from updates of its cross section values. Right: The curves become nearly indistinguishable when the drift velocity is plotted rather than the mobility.



In the second case the electron is lost. The abundant excitation modes of CO₂ enhance the process of Eq. (7). Therefore, high requirements for the oxygen purity of the gas mixture in the TPC are indispensable.

The electron attachment can be parametrized as a function of the drift length and therefore drift time by

$$N(t) = N_0 \cdot e^{-p(M)p(O_2)Kt}, \quad (8)$$

where $p(M)$ is the operation pressure of the counting gas, $p(O_2)$ is the partial pressure of the oxygen impurity, and K is the electron attachment coefficient. The average value of $p(O_2)$ during the beam time in the year 2000 was 0.011 mbar, i.e. 11 ppm, while the operation pressure $p(M)$ in the TPC was about 1 mbar above the atmospheric pressure. It is clear from Eq. (8) that the effect of the electron loss due to attachment increases with the drift length.

The decrease of the induced signal with the drift time was parametrized with an exponential description (Eq. 8) and corrected individually for each of the 20 planes in the TPC in units of one hour data taking. The correction accounted for different particle composition varying as a function of the polar angle θ .

7 Readout chambers

The readout chambers are conventional Multi Wire Proportional Chambers. The electrode configuration is shown in Fig. 16. Thin parallel and equally spaced anode wires are sandwiched between a cathode wire plane and the pad plane. The anodes are operated at about 1.3 kV. The cathode wires are held at ground potential. With the given gas mixture this corresponds to an electron amplification of about $8 \cdot 10^3$. The potential of the gating grid, located 6 mm above the cathode wire plane, controls the passage of electrons and ions. When the gate is closed electrons from the drift volume cannot reach the anode wires. It also prevents the backdrift of ions generated in the avalanche process from reaching the drift volume. The gating grid is operated at an offset potential of $U_{offset} = -140$ V to ensure full transparency to drifting electrons. In the closed mode, an additional bias potential of $U_{bias} = \pm 70$ V is applied between neighboring wires of the gating grid. This ensures full opacity to drifting electrons and limits the ion leakage fraction to about 10^{-4} . Only at a trigger signal the gating grid is switched to the transparent mode at $U_{bias} = 0$ V for the duration of the maximum drift time of electrons, using fast gating grid pulsers based on MOSFET technology [23].

7.1 Field configuration

The electric potential map of a readout chamber with the gating grid open, calculated with the simulation package GARFIELD [24], is shown in Fig. 17. A gating grid potential of -140 V would match exactly a drift field defined by the -30 kV cylinder potential on one side and the grounded cathode

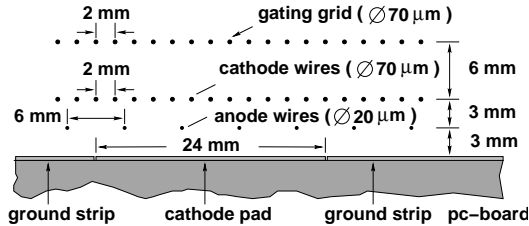


Fig. 16. Cross-section of a readout chamber. The wires are stretched in azimuthal direction above the pad plane. The anodes are operated at about 1.3 kV, the cathodes are grounded. The potential of the gating grid controls the passage of electrons and ions.

plane at $x = 1314$ mm on the other. However, the leakage of the anode field through the cathode plane, which effectively shifts the 0 V plane by about 2 mm, and the fact that the actual cylinder potential is -29.2 kV, led to a slight mismatch, visible at the gating grid plane at $x = 1308$ mm. The distortion is more significant in ϕ close to the edge of the chamber, where the distance from the cylinder is larger. The resulting potential at the gating grid plane at $r = 1308$ mm, averaged in z over the distance between two grid wires, acquires values between -110 V and -126 V, depending on z and ϕ . The potential map $V_{gg}(z, \phi)$ was used as the boundary condition when calculating the three-dimensional electric potential map (Sect. 4). It has been checked that a variation of the anode potential within 1300–1400 V has no visible impact on the drift field.

7.2 Gating grid

The performance of the gating grid is characterized by the transparency T , which is the ratio of electric flux lines crossing the gating grid plane to the total number of electric flux lines between gating grid wires and HV-cylinder. A measurement of the gating grid transparency as a function of the offset

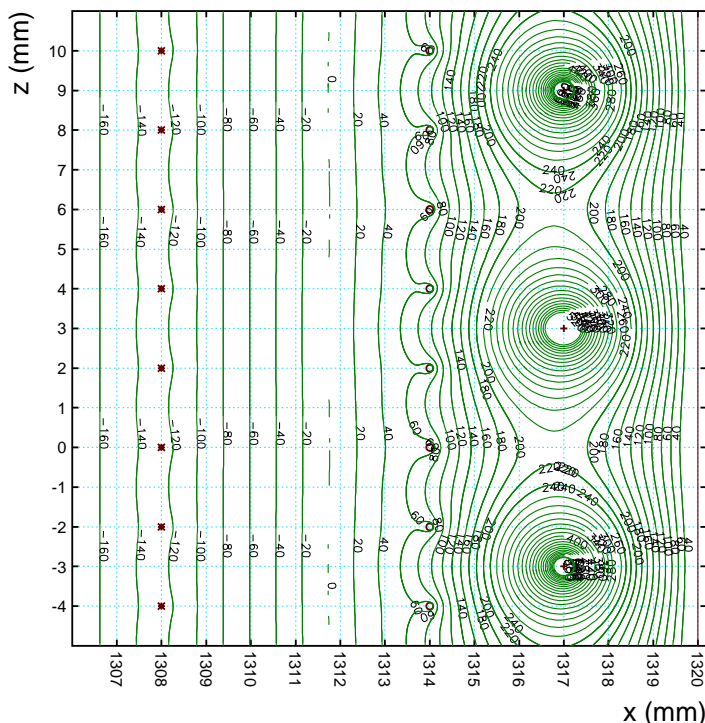


Fig. 17. Equipotential lines inside the readout chamber calculated with the GARFIELD package. The gating grid wires at $x = 1308$ mm and the cathode plane wires at $x = 1314$ mm are kept at -140 V and 0 V, respectively. However, because of the leakage of the field, the effective -140 V and 0 V planes are at $x = 1307.5$ mm and 1311.7 mm, respectively.

voltage U_{offset} is shown in Fig. 18, using a ^{55}Fe source and cross-checked with laser events [25]. The tests have been performed in static mode ($U_{bias} = 0$) without magnetic field using an anode wire voltage of $U_a = 1.4\text{ kV}$ and a voltage of $U_{HV} = -29.2\text{ kV}$ for the HV-cylinder. The data shows a saturation of the transparency at an offset voltage of about -90 V . The minimal offset voltage needed for full transparency depends linearly on the voltage of the HV-cylinder, as shown by the inset in Fig. 18.

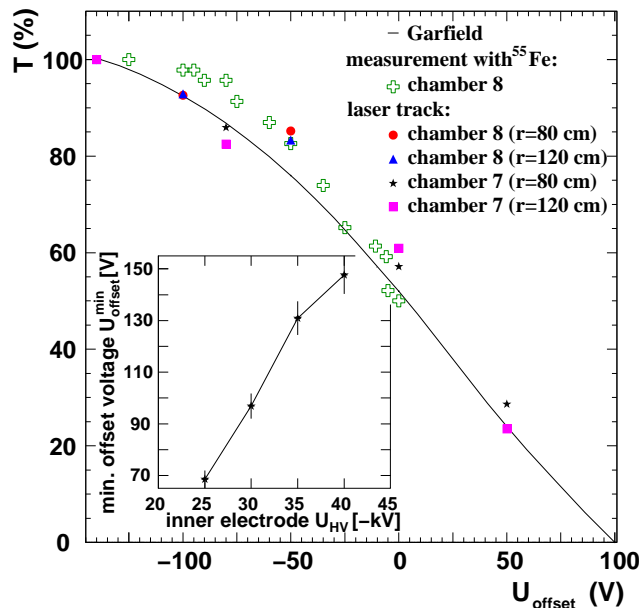


Fig. 18. Measurement of the gating grid transparency as a function of the offset voltage for a gas mixture of Ne/CO₂ (80%/20%). Saturation is reached at an offset voltage of about $U_{offset} = -90\text{ V}$. The minimal offset voltage needed for full transparency depends linearly on the voltage of the HV-cylinder (figure inset).

Fig. 19 shows the transparency as a function of the alternating bias voltage U_{bias} superimposed on the offset voltage [25]. The measurement was performed under the same conditions as described above using an offset voltage of $U_{offset} = -140\text{ V}$. The gating grid was closed with a bias voltage of about 60 V . Also the alternating bias voltage depends linearly on the voltage of the HV-cylinder, as can be seen in the inset in Fig. 19.

The magnetic field has an influence on the transparency of the closed gating grid. Due to the radial component B_r of the magnetic field with respect to the drift direction, electrons precess around their drift line defined by the electric field. This precession, in addition to diffusion, enables some electrons to pass the gating grid in spite of it being closed. GARFIELD simulations depicted in Fig. 19 show that a higher bias voltage has to be used in presence of a magnetic field to achieve the same transparency.

For the CERES TPC the radial component B_r of the magnetic field changes as function of the longitudinal coordinate z (cf. Fig. 11). This implies a dependence of the closing efficiency of the gating grid along the beam axis. However,

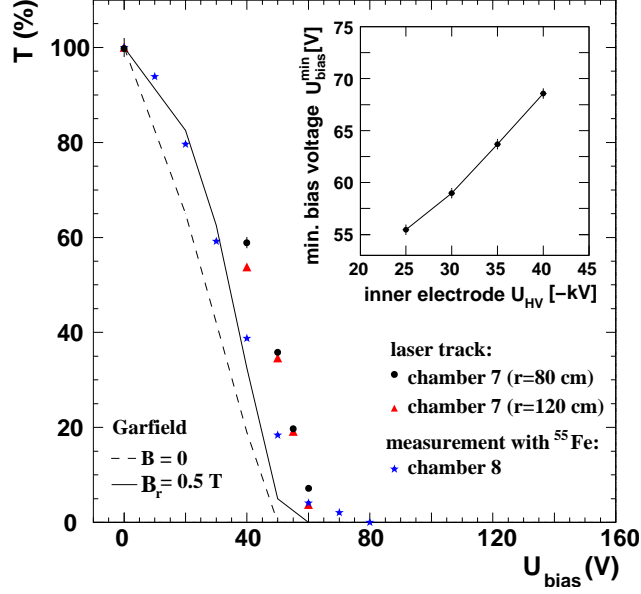


Fig. 19. Measurement of the gating grid transparency as a function of the alternating bias voltage for a gas mixture of Ne/CO₂ (80%/20%). The gating grid is closed at about $U_{bias} = 60$ V. The bias voltage depends linearly on the voltage of the HV-cylinder (figure inset). GARFIELD calculations show the influence of the magnetic field and the CO₂ concentration on the efficiency of the closed gating grid.

due to the weak magnetic field of at most 0.5 T used in the TPC and the cool properties of CO₂-based mixtures, the overall dependence of the closing efficiency of the gating grid on B_r is small ($\Delta U_{bias}^{min} = 6.6$ V/0.5 T), as confirmed by measurements. During operation a high value of $U_{bias} = 70$ V was chosen together with an offset voltage of $U_{offset} = -140$ V.

7.3 Gating grid settling time

The gating grid represents a capacitance C_{gg} . Thus, the opening happens with finite settling time τ_{gg} after receiving a trigger signal:

$$\tau_{gg} = f \cdot Z_0 \cdot C_{gg}. \quad (9)$$

$Z_0 = 50 \Omega$ is the impedance of the RG58 cable providing the voltage to the gating grid. The factor $f = 4.6$ is applied to describe when the signal reaches 99% of its maximum value. The capacitance of the gating grid is given by:

$$C_{gg} = C_0 + 2 \cdot C_M. \quad (10)$$

C_0 is the capacitance of the gating grid with respect to the cathode wire grid and C_M is the capacitance between the individual wires of the gating grid, resulting in an expected value of $C_{gg} \approx 8.1$ nF and, using Eq. (9), in $\tau_{gg} = 2 \mu\text{s}$. The capacitance between the gating grid and the HV-cylinder is small and can be neglected.

A capacitance measurement of C_0 and C_M resulted in $C_{gg} = 6.6 \text{ nF}$. The settling time was measured with a noise analysis of the readout channels of events without target interaction (empty events), resulting in $\tau_{gg} = 2.4 \mu\text{s}$, in good agreement with the expectations.

7.4 Pad plane

The TPC has 16 modular readout chambers, each having a total size of $2000 \times 518 \text{ mm}^2$ and 48×40 readout channels. The pad planes are composed of five printed circuit boards shown in Fig. 20 with an etched readout pad structure on the front side connected to the readout traces on the rear side.

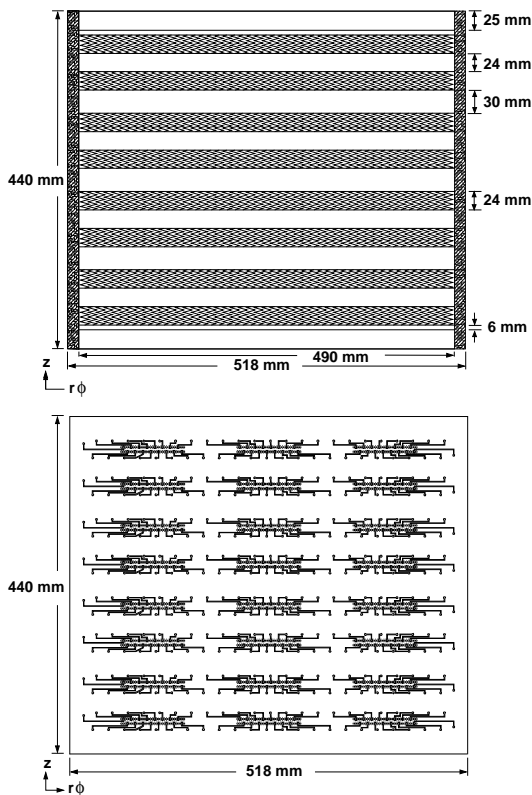


Fig. 20. Top: Pad side of a pad plane. Bottom: Readout side of a pad plane.

The printed circuit board is made of 3.2 mm thick FR4 material with a gold plated ($0.09^{+0.1}_{-0.1} \mu\text{m}$ Au, $4.5^{+0.1}_{-0.2} \mu\text{m}$ Ni) copper surface ($18 \mu\text{m}$ Cu) and a resulting tolerance of its total thickness of $^{+0.32}_{-0.30} \text{ mm}$. The readout pad structure is produced with an accuracy of $\pm 50 \mu\text{m}$ in each dimension. The gaps between conductive areas are etched with a width of $125 \mu\text{m}$ at the pad side and $250 \mu\text{m}$ at the readout side of the board. Each readout channel is connected via plated through holes ($\varnothing 1.0 \text{ mm}$) to the rear side of the printed circuit board to pick up its signal. To guarantee gas tightness, each hole is sealed with epoxy. The pad rows are separated from each other by ground strips of alternating thickness of 24 mm and 30 mm. This large spacing between the pad rows was chosen

due to financial constraints and concerns with the data volume and therefore readout speed. Furthermore, only half of the 40 pad rows were equipped with Front-End Electronics (FEE). The area of the three inner pad planes is $390 \times 518 \text{ mm}^2$, and of the two outer ones is $415 \times 518 \text{ mm}^2$. For mechanical stability the printed circuit boards are glued onto a 5 mm thick G10-backplate. The backplate has cut-outs for the connectors of the readout electronics and is itself glued onto an Al frame. The ledges holding the wires are glued onto the pad side of the printed circuit boards.

7.5 Pad response

The CERES TPC employs chevron-shaped cathode pads to perform centroid determination of a spatially extended induced charge signal by geometric charge division (Fig. 21). Compared to the commonly used rectangular pads, chevron pads allow a substantially larger readout node spacing. Based on theoretical calculations and experimental measurements [26] the displaced single chevron version (Fig. 21 (b)) was chosen.

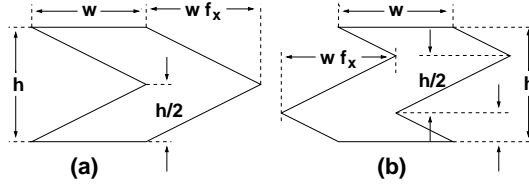


Fig. 21. Pattern of a centered (a) and displaced (b) single chevron pad. Chevron pads allow a larger readout node spacing than rectangular pads. For the CERES TPC the chevron version (b) was chosen.

The error of position measurement $\delta_{r\phi}$ has statistical and systematical contributions:

$$\delta_{r\phi} = \delta_{stat} + \delta_{syst}. \quad (11)$$

Here, $r\phi$ refers to a point on the pad plane in ϕ -direction. The statistical terms are given by the finite number statistics of the electrons created in the drifting electron cloud (δ_{diff}), the track angle α with respect to the pad direction ($\delta_{\tan(\alpha)}$), and an additional smearing of the electron distribution close to the anode wire where the electron trajectory is crossing the radial component of the magnetic field ($\delta_{\vec{E} \times \vec{B}}$). The overall noise behavior is contained in δ_0 ,

$$\begin{aligned} \delta_{stat}^2 &= \delta_{diff}^2 + \delta_{\tan(\alpha)}^2 + \delta_{\vec{E} \times \vec{B}}^2 + \delta_0^2, \\ \delta_{diff}^2 &\sim 1/l; \quad \delta_{\tan(\alpha)}^2 \sim l; \quad \delta_{\vec{E} \times \vec{B}}^2 \sim d; \quad \delta_0^2 \sim const., \end{aligned} \quad (12)$$

where l refers to the length of the chevron pads and d to the anode wire spacing. With the specific geometry of the CERES TPC and the Ne/CO₂ (80%/20%) gas mixture, calculations using Eq. 12 showed that for $l = 24 \text{ mm}$

and $d = 6$ mm the statistical position error can be minimized to $200 - 400 \mu\text{m}$ depending on the drift distance. Four of these displaced single chevron structures, with four anode wires running across, are connected to one single readout channel (Fig. 22). The width of a chevron pad has been fixed to $w = 10.3$ mm. Thus, each readout element contains 46 complete chevron pads in ϕ -direction and two half sized chevron pads at the edge.

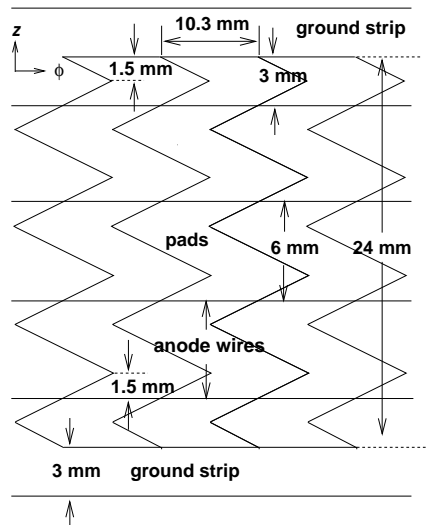


Fig. 22. Layout of the cathode pads. One readout channel is composed of four single chevron pads shown in Fig. 21 (b).

The finite granularity of the readout pads introduces an additional systematical error $\delta_{\text{sys}} = r\Delta\phi$ to the error of position measurement. This contribution can be minimized by optimizing the overlap factor f_x as defined in Fig. 21. The induced cathode charge distribution f can be described by a two-dimensional empirical expression [27]:

$$f(\lambda) \simeq K_1 \cdot \frac{1 - \tanh^2(K_2\lambda)}{1 + K_3 \tanh^2(K_2\lambda)},$$

with $K_1 = \frac{K_2\sqrt{K_3}}{4 \arctan \sqrt{K_3}}$; $K_2 = \frac{\pi}{2}(1 - 0.5\sqrt{K_3})$; $\lambda = \frac{x}{L}, \frac{y}{L}$. (13)

Here x and y are the coordinates in the pad plane, L is the anode-cathode spacing. K_3 is a parameter depending on the chamber geometry (anode-cathode spacing and anode wire spacing) in $r\phi$ - and z -direction. For the CERES-TPC the values are $K_3^{\text{r}\phi} = 0.655$ and $K_3^z = 0.805$. The distribution of Eq. 13 was used to integrate the induced charge over each pad.

The uniform irradiation response UIR is defined as the inverse of the derivative of the reconstructed centroid $r\phi_{\text{rec}}$ as a function of the original position $r\phi$:

$$r\phi_{\text{rec}} = f(r\phi); \text{ UIR}(r\phi) = 1/f'(r\phi). \quad (14)$$

One of the commonly used measures of nonlinearity is the differential nonlinearity DFNL defined as:

$$DFNL = \frac{UIR_{max} - UIR_{min}}{(UIR_{max} + UIR_{min})/2}. \quad (15)$$

Calculations of the DFNL as a function of the overlap factor f_x for the CERES TPC chevron pattern showed that the nonlinearity can be minimized by choosing $f_x \simeq 1.0$, reducing the remaining position error $r\Delta\phi$ to $\pm 6 \mu\text{m}$. Previous simulations and measurements [26] showed that the ideal value of $f_x = 1.0$ has to be increased to $f_x = 1.05$ in order to take the finite gap between adjacent pads into account. It has to be noticed that the above considerations are ideal, i.e. noise present in the induced charge on a cathode pad is not considered as well as counteractive measures such as pedestal subtraction. The measured position error will be described in Sect. 7.6.

The pad response function describes the induced charge on a cathode pad as a function of its distance to the charge centroid. Fig. 23 shows a measurement [25] from a readout chamber using an ^{55}Fe source. It shows the charge

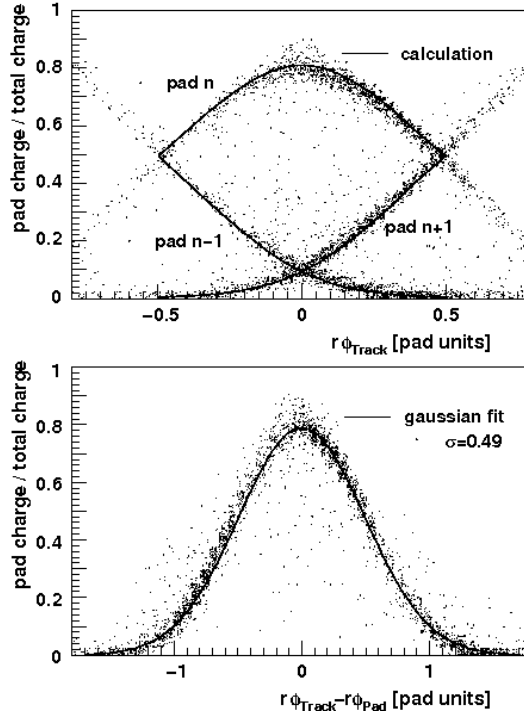


Fig. 23. Top: Measured charge sharing between three adjacent pads and the corresponding calculation. Bottom: Pad response function with a Gaussian width of 0.49 pad units, corresponding to 5.05 mm.

sharing between three adjacent pads and the corresponding pad response function. The charge sharing was calculated integrating Eq. 13 and shows good agreement with the measurement. The pad response function can be described

in good approximation by a Gaussian with $\sigma = 0.49$ pad units (one pad unit = 10.3 mm).

7.6 Correction for the pad response nonlinearity

To determine the remaining small nonlinearity in the pad response it was assumed that the true angle ϕ_{true} can be approximated by the azimuthal angle of a track ϕ_{track} at a given space point. This assumption is justified by the fact that a track is fitted through 12–20 space points and thus minimizes position uncertainties. The nonlinearity depends on the number of pads on which a signal is induced (Fig. 24, top). The angular difference between ϕ_{track} and the reconstructed space point ϕ_{hit} plotted vs. a fraction of a pad shows a maximum azimuthal position distortion of about 0.3 mrad for 2 pad clusters and about 0.1 mrad for 3 pad clusters [28], respectively. The corresponding correction was performed separately for positive and negative magnetic fields via look-up tables containing the position uncertainties. The result of the correction is shown in the bottom of Fig. 24.

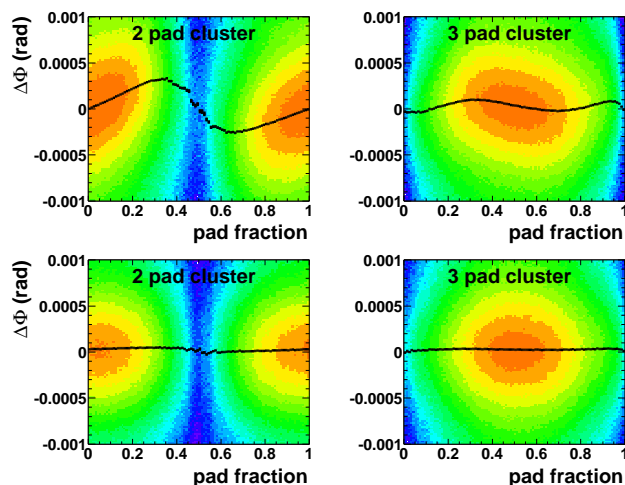


Fig. 24. Top: Angular difference $\Delta\phi = \phi_{track} - \phi_{hit}$ vs. a fraction of a pad. The remaining nonlinearity of the pad response is shown as bin-by-bin average of the entries in the color scatter plots. Bottom: Data after nonlinearity correction. The example is plotted for a positive magnetic field in the TPC.

7.7 Correction for anode wire positions

The precision of the adjustment of the anode wires above the cathode pad planes is finite. Deviations from the nominal positions were calibrated using a sample of data taken in the absence of a magnetic field. For each plane and each chamber the difference of the azimuthal angle between the track and its hits $\Delta\phi = \phi_{track} - \phi_{hit}$ was plotted versus the pad number (Fig. 25, top) [28]. Again ϕ_{track} stands for the true azimuthal angle ϕ_{true} .

The observed offsets depend linearly on the pad number and were parametrized with a polynomial of first order. The linear dependence has its origin in the chevron-shaped structure of the cathode pads. If the position of an anode wire above the pads is shifted in beam direction (parallel to the z -coordinate) the charge sharing between the pads must necessarily change. This in turn influences the determination of the centroid of a hit. An offset of $\Delta\phi = 1$ mrad corresponds to an anode wire shift of about $\Delta z = 0.37$ mm. The azimuthal hit position ϕ_{hit} was corrected via a look-up table (Fig. 25, bottom).

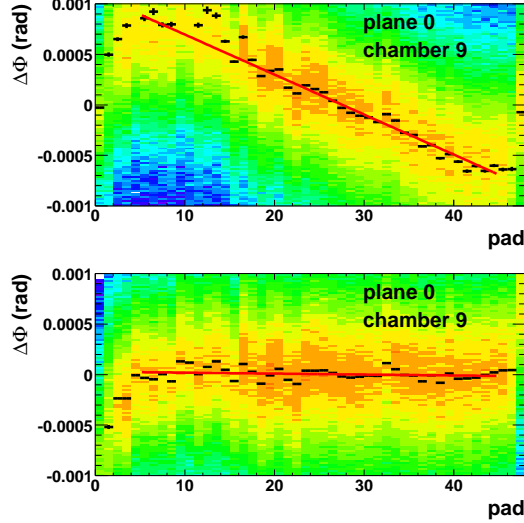


Fig. 25. Top: Shifts of anode wires result in a linear dependence of $\Delta\phi = \phi_{track} - \phi_{hit}$ vs. pad number. This is shown by the bin-by-bin average of the entries in the color plots. Bottom: The anode wire positions were corrected individually for each plane and each chamber via a look-up table.

8 Readout electronics

The data acquisition chain of the TPC starts with the Front-End Electronics (FEE) comprising a Preamplifier/Shaper (PASA) and a Switched Capacitor Array (SCA), an analog memory to record the analog output signal of the amplifier. Both chips were implemented in the $0.8\mu\text{m}$ AMS CMOS process [29]. The FEE-boards are directly mounted on the readout chambers of the TPC.

An overview of the CERES readout system implemented for the beam time in 2000 is shown in Fig. 26 [30]. The analog output signals from the FEE-boards are sent via 14m long coaxial cables to the Front-End Digital Cards (FEDC) [31,32] where the signal is digitized. To handle the data of two TPC chambers three FEDC modules are necessary (one FEDC per 640 cathode pads) and they are grouped in one 9U VME crate close to the TPC. The digitization process is clocked by an external clock signal which is provided

by a central TPC Clock Module.

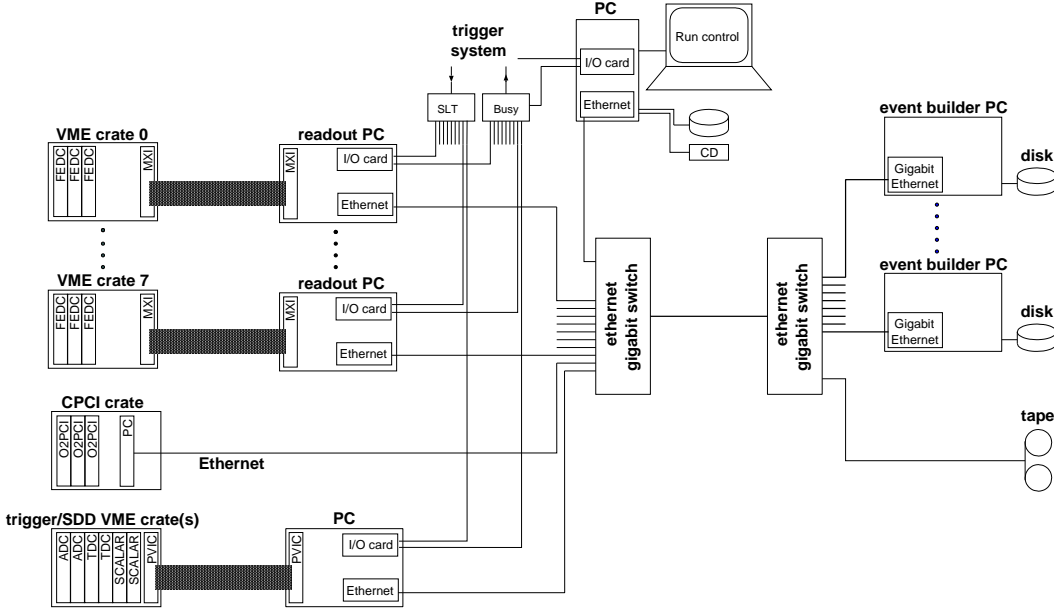


Fig. 26. Overview of the CERES data acquisition in 2000. 24 FEDC modules handle the data of the 16 TPC chambers. The FEDC VME crates are connected via MXI-buses to 8 readout PCs, which in turn are connected via Gigabit Ethernet to event builder PC in the CERN Central Data Recording facility.

The FEDC VME crates are connected via MXI-buses (Multisystem Extension Interface) to readout PCs. Eight readout PCs were needed to read the 16 TPC chambers. During the heavy-ion beam time in 2000 the SPS beam was extracted and steered onto the target for 5 s followed by a pause of 14 s. During extraction all data were collected in the readout PCs. The interval between bursts was used to send the data via Gigabit Ethernet connection to one of the seven event builder PCs, located in the CERN Central Data Recording facility (CDR). There the data of one event coming from different detector systems were merged into one single data block and saved to disk. A tape daemon asynchronously archived the data on tape.

The data of the SDD and the RICH detectors from the compact PCI modules (CPCI) are collected in the main memory of an embedded PC which is plugged into the CPCI crate. From there the data is sent via Ethernet to the event builder.

The discriminators, coincidences, and downscalers used for the trigger logic, ADCs and TDCs of the beam related photomultiplier detectors, and counters of various beam and trigger signals are sitting in three VME crates located in the grillage. These crates are daisy-chained via VME extenders, and connected via a PVIC (PCI Vertical Interconnect) interface to another readout PC.

The start of the readout was triggered by an external signal applied to an input channel of an I/O-card plugged in each readout PC. After receiving

a trigger, a readout PC would set a busy signal on an output channel of its I/O-card. A logic OR of all busy signals was used to inhibit new triggers. After all data were sent to the readout PC the busy signal was removed.

The typical event size for a central Pb-Au collisions at 158 GeV/c per nucleon was 500 kB. From all detectors the average busy duration, i.e. the average time needed to get the event into the memory of a readout PC, was largest for the TPC with 5.7 ms. With a beam intensity of 10^6 per burst, with the requirement of no other beam particle within $\pm 1 \mu\text{s}$, and with the centrality trigger of 7% the event taking rate was 300–400 per burst.

8.1 Preamplifier/Shaper

A schematic drawing of the custom PASA chip is shown in Fig. 27 [29]. It comprises a charge-sensitive preamplifier with a semi-Gaussian shaper and tail suppression. In contrast to common designs which use a pulsed reset, this amplifier is continuously sensitive. This is important in a high track density environment typical for a heavy ion collision.

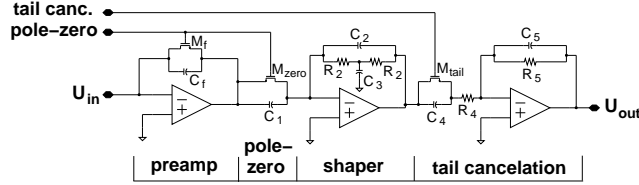


Fig. 27. Schematics of the PASA comprising a charge-sensitive preamplifier with a semi-Gaussian shaper and tail suppression. The PASA is part of the Front-End Electronics of the TPC.

A feedback resistor M_f continuously discharges the integration capacitor C_f with a decay time $t_{decay} = C_f M_f$. The value of M_f is a trade-off between noise performance and the capability to process events with high occupancy. For a peaking time $t_{decay} = 400 \text{ ns}$, noise considerations dictate a feedback resistance $M_f > 4 \text{ M}\Omega$. The only way to implement such a high resistance in CMOS technology is by using the associated drain-source resistance R_{ds} of a MOSFET transistor. The value of R_{ds} depends on the biasing conditions of M_f . It decreases as the gate-source voltage V_{gs} of M_f increases. This dependence is an advantage in our case as signal charges increase V_{gs} : the integration of small charges results in small V_{gs} swings, thus $R_{ds} \approx R_{ds,DC}$. When this value is large enough, it prevents deterioration of the noise performance. Conversely, large charges are discharged with a faster decay time and the baseline of the preamplifier is quickly restored. Even more important is that undesired large signals (e.g. from δ -electrons) collected on TPC pads are transferred onto C_f and quickly discharged, minimizing dead time.

In case of a conventional pole-zero cancellation, the dependence of R_{ds} on the injected charge Q_{in} would deteriorate the linearity of the PASA. Here, an adaptive pole-zero cancellation scheme was used to suppress the pole as-

sociated with R_{ds} and C_f . The transistor M_{zero} is biased in the same way as M_f during the discharge of C_f . The zero associated to the network $M_{zero}-C_1$ adapts itself dynamically to accurately cancel the pole associated with the network C_f-M_f .

The peaking time of the shaper can be adjusted between 140 and 580 ns and the tail suppression can be varied over a range of 0.1–1.5 μ s to cope with different input signals. The gain of the preamplifier can be adjusted from 35–110 mV/fC.

8.2 Switched Capacitor Array

During the drift time of the TPC the output of the PASA is sampled and stored in an analog memory (SCA) at a rate of up to 14 MHz. Fig. 28 shows the simplified schematics of this device. The SCA chip contains 16 channels, each with 256 individual samples. A 16-to-1 analog output multiplexer permits the use of a single external Analog-to-Digital Converter (ADC) per chip. The SCA is operated in voltage-read-voltage-write configuration which has the benefit that the output is independent of the exact value of the storage capacitor. Each memory cell consists of a 1.4 pF double poly capacitor connected by two transmission gates to the common lines. This scheme reduces parasitic capacitances during readout, when the storage cells are switched in the feedback loop of an operational amplifier. Without this second switch the read-amplifier would charge the total capacitance of all bottom plates to the substrate. Because the two transmission gates are inherently less sensitive than single transistor switches, the clock feed-through and charge injections are further reduced. Only the differences of the capacitor voltages between the top and the bottom plates are relevant and over a small range of input voltages the noise influence is the same on both plates. Symmetrical layout and only complementary signals running near analog cells ensure low switching noise caused by digital signals.

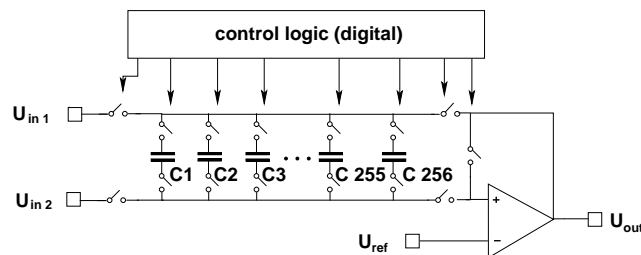


Fig. 28. Schematics of the SCA. The SCA is an analog memory to record the analog output signal of the PASA. It is part of Front-End Electronics of the TPC.

The digital part includes a shift register to sequentially address a column of cells. A programmable clock window prevents overlapping addressing signals to inhibit charge sharing between adjacent cycles. Two registers on the chip can be used to store a delay value for the start of the sampling and the maximum

number of readout channels. This allows to suppress data from tracks outside the conical acceptance of the tracks matching the other detectors.

8.3 *Front-End Digital Cards*

The digitization and further processing of the TPC signals is done on the FEDC-boards. These boards are realized as 9U VXI devices which can contain up to 48 readout channels. Each readout channels comprises a 10-bit ADC and a digital chip for signal processing (a modified version of the ALTRO chip for the ALICE TPC [33]) and processes the data from one FEE-board. For the CERES readout only 40 channels per FEDC were used.

Immediately after receiving a first-level trigger signal the SCA starts to sample the 16 outputs of the amplifier in parallel. This sampling phase is followed by the readout phase in which the stored analog values are dumped in a time-wise order. The data coming from the FEE-boards are digitized using the 10-bit ADC on the FEDC-board of which only the 9 most significant bits are used for further processing. Therefore, inside the ALTRO chip the signals are described by 9-bit codes (0–511). After converting the analog signal the data stream is demultiplexed according to the 16 channels of the preamplifier. The resulting 16 data streams are processed in parallel inside the ALTRO chip.

In the following processing steps the polarity of the signal is changed and the baseline is subtracted. After this subtraction the signal should be contained in the first half of the 9-bit range. Therefore the most significant bit can be omitted reducing the signal representation to 8-bit codes. Finally the signal undergoes zero suppression. Samples with a value smaller than a constant threshold (8-bit) are rejected. This threshold is stored in one of the control registers of the ALTRO chip. When a sample is found to be above the threshold, it is considered as the start of a pulse and stored in the central memory of the FEDC.

Because each ALTRO chip processes data coming from 16 readout channels with a maximum of 256 time samples, it was not possible to provide enough memory inside the chips to hold pedestal values for all samples. Instead, a scheme using a look-up table was implemented. The slight disadvantage of this scheme is the missing possibility to specify a threshold for zero suppression for all time bins. This restriction was evaded by adding the threshold (determined individually for each time bin) to the pedestal value and storing this combined value in the pedestal memory. The zero suppression value which is used to detect the start of a pulse was set to zero. With this scheme, not only the true baseline is subtracted from the signal but also the specific threshold. If the resulting value is above zero, the pixel is considered being part of the pulse. For the off-line analysis the additionally subtracted threshold had to be added again for each pixel.

8.4 Electronics response

Sixteen adjacent pads are processed in one FEE-board. Each pad row of a readout chamber is equipped with three FEE-boards. Fig. 29 shows the electronic noise behavior of a row of 48 pads in one readout chamber [25]. This noise behavior is caused by the different readout line capacitances (cf. Fig. 20, bottom). The correlation between circuit path lengths and noise behavior is shown in Fig. 30. A straight line fit results in a noise level of $\sigma_0 = 1.12$ ADC counts for an isolated readout channel with zero readout trace length.

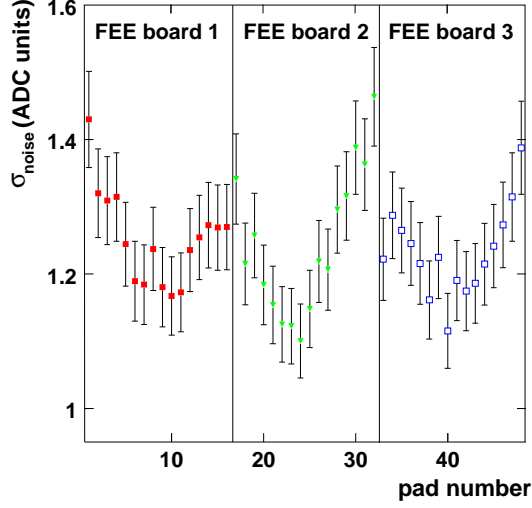


Fig. 29. Noise behavior of single readout channels in the three FEE-boards of one chamber caused by the different readout line capacitances.

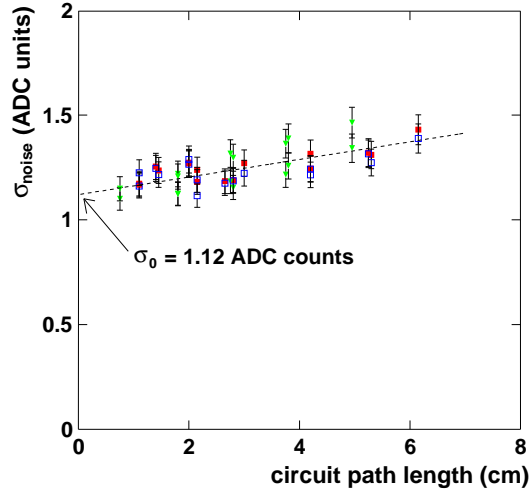


Fig. 30. Dependence of the noise behavior of a readout channel on its readout trace length. An isolated readout channel with zero readout trace length would have a noise level of $\sigma_0 = 1.12$ ADC counts.

The Equivalent Noise Charge (ENC) of the FEE-board electronics is given

by:

$$ENC_{out} = g_{SCA} \cdot \sqrt{(g_{PASA} \cdot ENC_{pad})^2 + ENC_{SCA}^2}. \quad (16)$$

In this equation $g_{PASA} = 1.5$ and $g_{SCA} = 1.6$ are the gains of the PASA and SCA, respectively. The measured $ENC_{out} = 1.12$ ADC counts correspond to $1288 e^-$ noise charge (1 ADC counts = $1150 e^-$), which in turn corresponds to a noise value of $ENC_{pad} = 498 e^-$. The ENC is a function of the peaking time τ_{peak} where the signal reaches its maximum. Theoretical considerations of the serial ($\propto 1/\sqrt{\tau_{peak}}$), parallel ($\propto \sqrt{\tau_{peak}}$), and white (independent from τ_{peak}) noise contributions to the ENC yield an expected cathode pad noise value of $ENC_{pad} \approx 445 e^-$ at a peaking time $\tau_{peak} = 340$ ns and a cathode pad capacitance $C_{pad} = 12$ pF [34]. This is in good agreement with the above measurement.

8.5 Effect of the trace length on the time measurement

The reconstructed position of the high voltage cylinder, adjusted to its true value by shifting and tilting the chambers as described in Sect. 4.4, still shows a periodic oscillation when plotted vs. the pad number modulo 48, i.e. across a chamber (Fig. 31, bottom). The three bumps reflect the three FEE-boards

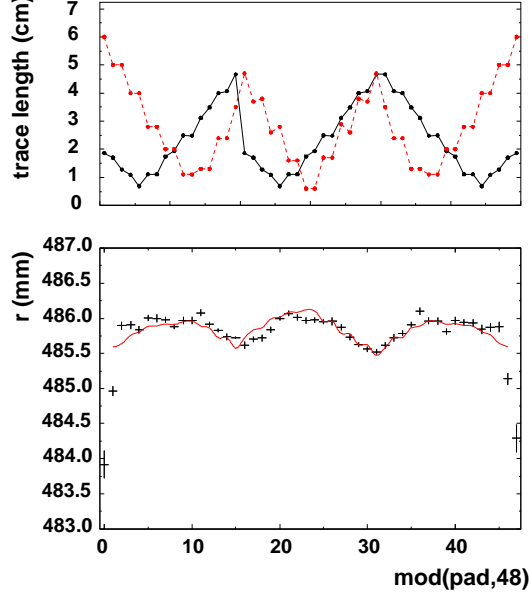


Fig. 31. Top: Trace length on the FEE-board (solid) and on the pad plane (dashed). Bottom: Periodic oscillation in the reconstructed radius of the HV-cylinder. The line is a linear combination of the pad plane and FEE-board trace lengths from the upper plot, with the two coefficients optimized to fit the data.

of 16 pads each and originate from the pad-to-pad variation of the length of the trace within the pad plane $L_{ppl}(pad)$ and on the FEE-boards $L_{fee}(pad)$

(Fig. 31, top). The trace length differences are much too small to have any impact on the signal propagation time. However, they affect the measured drift time via the capacitance and the signal shape. As shown by the line in the bottom of Fig. 31 the deviation can be reproduced by a linear combination of the two trace length distributions:

$$\Delta r(pad) = 0.10 \cdot L'_{ppl}(pad) + 0.03 \cdot L'_{fee}(pad) \quad (17)$$

where the reconstructed radius correction Δr is in mm and the trace lengths L'_{ppl}, L'_{fee} are in cm. The index pad goes from 0 to 47 and measures the azimuthal position within one chamber. The trace length at the azimuthal center of the chamber has been subtracted:

$$L'_{ppl}(pad) = L_{ppl}(pad) - \frac{L_{ppl}(23) + L_{ppl}(24)}{2}, \quad (18)$$

$$L'_{fee}(pad) = L_{fee}(pad) - \frac{L_{fee}(23) + L_{fee}(24)}{2}. \quad (19)$$

For laser events the best fit is obtained with the two coefficients in Eq. 17 being equal to 0.19 and 0.24, respectively. The difference between the nuclear collisions and the laser events is presumably caused by a different signal shape.

8.6 Anode induction

Fig. 32 shows an average of a large number of pedestal subtracted laser events [25]. Clearly visible is the strong laser peak and the signals from electrons released from the inner cylinder by UV stray light at large time bins. Besides the baseline shift that follows the laser signal in temporal direction there is also a sagging of the baseline of the neighboring pads. These are signals induced by the group of anode wires where the avalanche took place [35].

Whenever gas amplification happens at an anode wire, the resulting drop of the anode wire voltage is determined by the amount of charge Q_{amp} that has been deposited during the amplification and by the capacitance C_{aw} of the anode wire with respect to the surrounding electrodes:

$$\Delta U = \frac{Q_{amp}}{C_{aw}}. \quad (20)$$

The measured pulse height PH_{signal} of the signal can be calculated from the actual charge at the anode wire:

$$PH_{signal} = \frac{256}{2.1[\text{mV}]} \cdot Q_{amp}[\text{fC}] \cdot g_{electronics}[\text{mV/fC}] \cdot \epsilon_{pad} \cdot \epsilon_{PASA}. \quad (21)$$

Q_{amp} is given by the product of the primary ionization Q_{prim} and the gas gain, $g_{electronics}$ is the gain of the electronics. The factor $\epsilon_{pad} = 0.3$ takes into

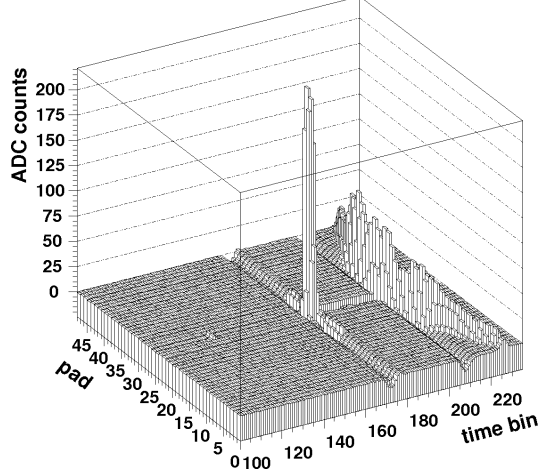


Fig. 32. Average of many laser events in pad-time space. The laser peak is followed by a baseline shift in temporal direction, as well as a sagging of the baseline on neighboring pads. The structure seen at large drift time is caused by UV stray light knocking out electrons from the inner cylinder.

account that only about 30% of the signal couples to the cathode pad plane, while the efficiency loss factor $\epsilon_{PASA} = 0.5$ occurs as a consequence of the finite integration time of the PASA. The factor $\frac{256}{2.1[\text{mV}]}$ converts the pulse height from mV to ADC counts.

On the other hand, each single cathode pad has a capacitance C_{pad-aw} with respect to the anode wire grid. Therefore, a drop of the anode wire voltage ΔU will induce a charge

$$q_{crosstalk} = C_{pad-aw} \cdot \Delta U = \frac{C_{pad-aw}}{C_{aw}} \cdot Q_{amp} \quad (22)$$

on the cathode pad. This charge can be related to the measured pulse height signal $PH_{crosstalk}$:

$$PH_{crosstalk} = \frac{256}{2.1[\text{mV}]} \cdot q_{crosstalk}[\text{fC}] \cdot g_{electronics}[\text{mV/fC}] \cdot \epsilon_{PASA}. \quad (23)$$

Note that the factor ϵ_{pad} does not enter because the coupling between anode wire grid and pad has already been explicitly taken into account by the capacitance C_{pad-aw} .

According to Eq. 22, the magnitude of the induced signals scales with the amount of charge that has been created by gas amplification in the same time bin. Making use of Eq. 21 to 23, the measured dip can be related to the sum of the visible positive pulses:

$$PH_{crosstalk} = \frac{1}{\epsilon_{pad} \cdot \epsilon_{signal}} \cdot \frac{C_{pad-aw}}{C_{aw}} \cdot PH_{signal}. \quad (24)$$

The factor $\epsilon_{signal} = 0.24$ takes into account that in the case of the CERES

TPC the pulse height corresponds to only 24% of the total charge deposited on the anode wires. This corresponds to the geometric fraction of the total signal which is read out (3 pad rows of 2.4 cm length, each in an anode wire group of 33 cm length). The capacitance C_{pad-aw} has been measured to be 0.27 pF. The anode wires of each chamber are powered by six HV-sectors, which are accessible from the backplate of the TPC. The capacitances C_{aw} of the six HV-sectors have also been measured and are listed in Table 1.

Table 1

Capacitances of the individual sense wire groups (HV-sectors).

| HV sector | cable length [cm] | capacitance C_{aw} [pF] |
|-----------|-------------------|---------------------------|
| 1 | 250 | 812 |
| 2 | 200 | 722 |
| 3 | 170 | 668 |
| 4 | 144 | 622 |
| 5 | 116 | 571 |
| 6 | 74 | 492 |

Fig. 33 shows the measured ratios $PH_{signal}/PH_{crosstalk}$ as a function of the capacitances of the individual anode wire groups. If Eq. 24 holds, one would expect a linear dependence in this representation, which is indeed suggested by the measurement. However, the magnitude of the effect is somewhat underestimated by Eq. 24, as indicated by the dashed line. The crosstalk effect was reduced by a factor 2.5 by placing additional capacitors of 5 pF in parallel to each individual anode wire group.

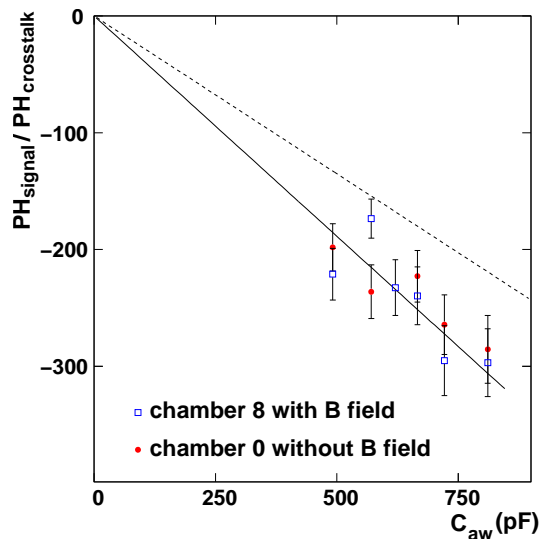


Fig. 33. Signal to crosstalk pulse height ratio as a function of the anode wire group. Also shown is the expectation from Eq. 24 (dashed line).

8.7 *Signal undershoot*

The baseline shift in temporal direction seen in Fig. 32 is caused by high-pass filters which are used to suppress leakage currents. High-pass filters work as differentiators for frequencies below the threshold frequency. Thus, a trailing edge of an incoming pulse will cause a negative outgoing pulse. This decreases the amplitude of pulses following in time.

The shape of the signal undershoot was parametrized with an exponential function and included as correction [36]. The correction assumes that the baseline shift is additive for subsequent clusters on a pad.

8.8 *Ion signal*

The electron avalanche occurs within less than $50\text{ }\mu\text{m}$ of the anode wires [37]. The process typically lasts for about 1 ns. The produced electrons are collected on the anode wires where they induce a negative signal. The remaining ions induce a positive signal on the readout pads. The ions drift towards the cathode wires about 1000 times slower than the electrons. The electric field strength is strongly weakened due to space charge and the drift velocity of the ions is further reduced. However, depending on the geometry of the chamber it may happen that the ions feel a second acceleration in proximity of the cathode wires where the electric field strength is again increasing. This late ion signal manifests itself in a negative induced signal on the cathode pads. According to GARFIELD simulations of the CERES TPC, the late ion signal is expected with a time delay of about $42\text{ }\mu\text{s}$ after the main signal.

A measurement of the late ion signal is shown in Fig. 34 [25]. The figure shows an average of many laser events taken without zero suppression and not corrected for pedestals. Taking into account that the ion drift velocity is not well known for electric fields prevailing in the vicinity of the cathode wires, the measured time delay of about $52\text{ }\mu\text{s}$ for the late ion signal is in good agreement with expectations. The lowering of the pedestals during the late ion signal is less than 0.8% as compared to the maximum signal and thus the correction of this effect was neglected.

8.9 *Pad-to-pad gain variations*

The pad-to-pad correction comprises all effects which cause gain variation from pad to pad, but also characteristics which extend over a whole electronic device. The top of Fig. 35 shows, as an example, the uncorrected pad-to-pad gain variation of the first plane of the TPC.

The most noticeable structure extends over groups of 48 pads corresponding to the chambers of the TPC. The periodic peaks can partly be explained by the sag of the anode wires. The wires are glued to the edge of a chamber. In

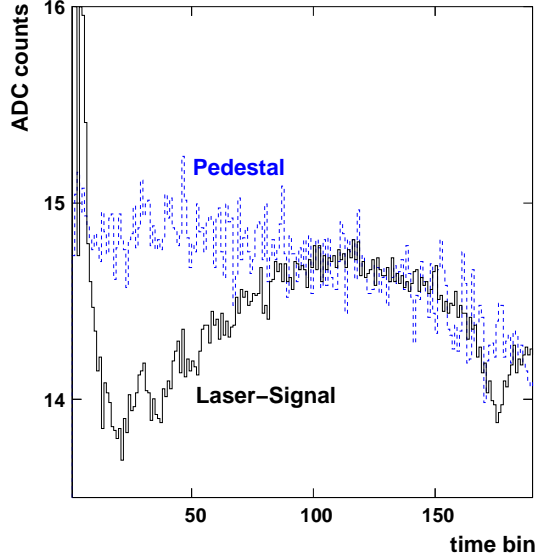


Fig. 34. Temporal development of the overlay of many laser events (solid line) and the corresponding pedestals (dashed line). The late ion signal is delayed by 175 time bins (1 time bin = 300 ns).

between these two fixed points the wires bend due to the electrostatic attraction towards the pad plane. This decreases the distance between the anode wires and the pads and thus a stronger signal is induced. The effect is strongest in the center of a chamber. It has also been observed that the gain drops at the end of the wires. Here the electric field differs from that of an infinite wire. Furthermore, the closing pads at the border of a chamber are smaller and have a different shape than the rest of the pads. This can be responsible for the dip at the edge of each chamber. Finally, the three-fold structure inside a chamber reflects the individual behavior of the front-end-boards.

The pad-to-pad gain variations have been studied in [36]. The correction is implemented in form of look-up tables and determined for each calibration unit. The effect of the correction is demonstrated in the bottom of Fig. 35.

9 Laser system

For calibration and monitoring purposes the CERES TPC is equipped with a laser system, shown in Fig. 36. A Nd:YAG laser with a small beam diameter of 2 mm and low divergence of below 0.5 mrad was chosen. With two frequency doublers the wavelength is converted from $\lambda = 1064$ nm to 266 nm. With a pulse duration of 4 ns and an energy of 10–20 μ J per pulse an ionization similar to the one caused by charged particles can be achieved inside the TPC with a repetition frequency of up to 10 Hz.

The laser light is sent into the TPC, parallel to its axis at different radii and azimuthal angles, using a mirror system mounted on the backplate of the TPC. The position of each laser ray is monitored with position sensitive diodes

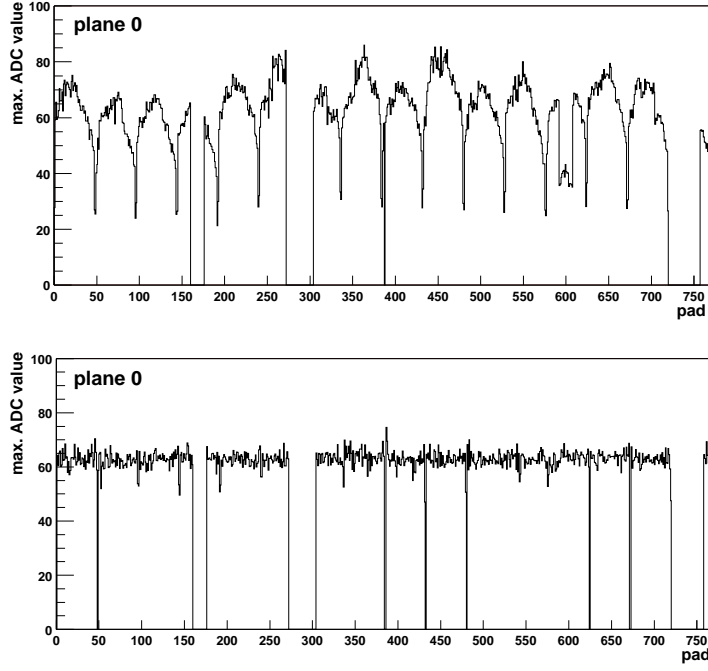


Fig. 35. Top: Uncorrected pad-to-pad gain variations. For the pad-to-pad gain correction the maximum amplitude of a hit is used, which is localized on a single pad. The maximum amplitude is corrected for the polar angle θ of the track. Bottom: Pad-to-pad gain variations after correction.

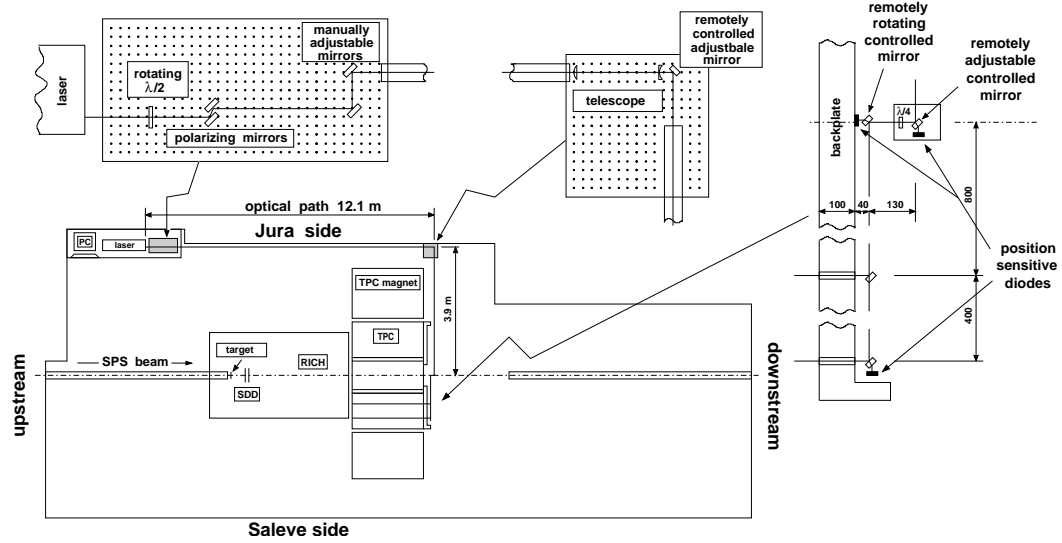


Fig. 36. Laser system of the CERES TPC. The laser light from a Nd:YAG laser is frequency doubled twice and sent into the TPC using a mirror system mounted on the backplate of the TPC.

located behind semi-transparent mirrors. The position of the laser ray and its angle at the entrance of the TPC are known within 0.25 mm and 0.5 mrad, respectively. A detailed description of the laser system can be found in [38].

10 Data analysis

The raw data recorded with the TPC during a beam period were processed into a suitable format for the subsequent data analysis. This section describes the basics of the reconstruction strategy and final calibration techniques.

10.1 Hit finding

The TPC has 20 planes with 768 pads arranged in azimuthal direction. The drift time, and thus the radial coordinate, is digitized in 256 time bins. The $20 \times 768 \times 256 \approx 4$ million pixels contain the linear amplitude information of the deposited charge in an 8-bit representation (cf. Sect. 8.3).

In order to reconstruct particle trajectories the first task to accomplish is to localize the passages of particles in the planes of the TPC, the so called hits. The hits are charged clusters, i.e. conglomerations of pixels with amplitudes $A > 0$. It is also possible that several hits overlap in one charged cluster. The hit finding procedure scans the time-pad pixel grid of each plane to find absolute maxima A_{max} within each cluster by first searching for local maxima in time direction and subsequently in pad direction [28]. In cases where the position of an absolute maximum within a cluster is ambiguous (i.e. several adjacent saturated pixels), the amplitude information from neighboring pixels is considered in the decision.

A study based on simulated and real events has shown that the area of deposited charge does not extend over more than five time bins and three pads. This defines an area of 15 pixels arranged around an absolute maximum within a cluster. Hits containing only one time bin row are discarded. The same applies for one pad clusters, with the exception of a hit being localized at the edge of a chamber or adjacent to a dead FEE-board.

To cope with the problem of overlapping hits, a counter variable f_i is allocated for each pixel i . It memorizes the sum amplitudes of absolute maxima from those hits which share the same pixel. The method is sketched in Fig. 37. In this way it becomes possible to assign weights to individual pixels by the ratio of the absolute maximum A_{max} of a certain hit and the counter variable f_i . For a given plane of the TPC the centroids for the time coordinate \bar{t} , and respectively for the pad coordinate \bar{p} , are given by:

$$\bar{t} = \frac{\sum_i A_i \cdot \frac{A_{max}}{f_i} \cdot t_i}{\sum_i A_i} \quad \text{and} \quad \bar{p} = \frac{\sum_i A_i \cdot \frac{A_{max}}{f_i} \cdot p_i}{\sum_i A_i}. \quad (25)$$

For a hit multiplicity between 17500 and 20000, about 80% of the hits are isolated, 17% are overlapping with one other hit and 3% are overlapping with two other hits. The advantage of calculating the centroid with weighted pixels as compared to a minimization procedure is a substantially decrease of computing time necessary for hit finding.

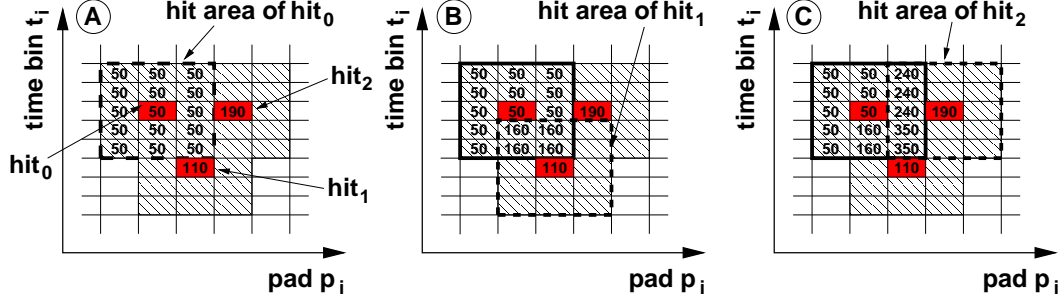


Fig. 37. Reconstruction of overlapping hits in the TPC. The counter variables memorize the value of the absolute maximum of the hit to which the pixel belongs. If a pixel is assigned to several hits, its counter variable is augmented by the absolute maxima of the overlapping neighbors.

10.2 Coordinate transformation

The detector specific hit coordinates ($pad, time, plane$) are transformed to spatial coordinates (x, y, z) via look-up tables. The transformation contains the information about the transport process of the charged clusters in the electric and magnetic fields inside the TPC.

The look-up tables are calculated using a Runge-Kutta method [39] that calculates the drift trajectory using in each point the drift velocity vector (Eq. 3), starting at the cathode plane. The drift between the cathode plane and the pad plane is absorbed in a ϕ -dependent time offset due the fact that each Front-End Electronic (FEE) channel had a slightly different capacitance. The difference between the MAGBOLTZ Monte Carlo drift [19] and the actual drift velocity vector is accounted for with a z - and $r(E)$ -dependent correction for the drift velocity component parallel to the electric field and the one parallel to $\vec{E} \times \vec{B}$.

10.3 Track finding

The tracking starts in one of the middle planes 5 to 15 where the hit density is lowest [10]. The hits in this region are subsequently combined with their closest matches in the two upstream and two downstream planes to determine the sign of the track curvature in ϕ -direction. The track curvature is linearly extrapolated to the remaining planes in which further hits are searched for within a narrow window of $\Delta\phi = 5.3 \text{ mrad}$ and $\Delta\theta = 1.4 \text{ mrad}$. The extrapolation contains z -dependent correction factors obtained from a GEANT [40] simulation of the TPC. The procedure stops if no further hit is found.

In a second step the track is fitted in several iterations with a second order polynomial using Tukey weights [41] to predict the position of missing hits. The window to search for hits is widened to $\Delta\phi = 15$ (10) mrad for upstream (downstream) hits. The complicated track trajectory due to the strong inhomogeneity of the magnetic field leads to a less accurate prediction of the fit

in the upstream direction for the low momentum (soft) tracks. This is taken into account by applying again correction factors in the last five planes, now depending on both the z -position of the plane and the curvature of the track. The search for hits is continued in higher planes in the case of missing hits.

A hit is only assigned to a single track, i.e. the sharing of hits between tracks is not allowed. The maximum number of hits per track is given by the 20 planes in the TPC. The minimum number is limited to 7 hits in order to reduce the contribution of imperfectly reconstructed or fake tracks.

10.4 Track fitting

Because of the inhomogeneous magnetic field in the TPC an analytical description of a trajectory is impossible. This problem is handled by using reference tables for the track fit in the ϕ - z and r - z planes. The reference tables contain the hit coordinates of Monte Carlo tracks from a GEANT [40] simulation of the TPC including the measured magnetic field configuration. The Monte Carlo tracks are generated in bins of 32 different ϕ angles in the range $-\pi < \phi < \pi$, 18 different η angles in the range $2.05 < \eta < 2.95$ and 8 different inverse momentum values in the range $-2 < q/p < 2 \text{ (GeV/c)}^{-1}$, where q is the charge of the simulated particle. The track segments in the TPC are fitted with a two-parameter fit assuming that the tracks originate from the vertex, and with a three-parameter fit taking into account multiple scattering which happens mainly in the mirror of the RICH2 detector. After several iterations, hits with large residuals $\Delta r > 0.4 \text{ cm}$ and $r\Delta\phi > 0.2 \text{ cm}$ are excluded from the fit. The distribution of initial and final ('fitted') number of hits per track is shown in Fig. 38. The average number of hits (fitted hits) per track is 16.5 (15.3) with a most probable value of 19 (18) hits. This means that on average one hit per track is excluded from the fit.

The single track efficiency of the TPC for positive pions traversing the detector at $\theta = 0.18 \text{ rad}$, i.e. at the center of the acceptance, is shown in Fig. 39 as a function of momentum [42]. The efficiency was determined by embedding Monte Carlo tracks in experimental central Pb-Au events. The efficiency drops steeply for tracks with a momentum smaller than 0.6 GeV/c . Tracks with $p > 1 \text{ GeV/c}$ are reconstructed with an efficiency of 96%. About half of the inefficiency there is caused by a row of not powered FEE-boards at $\phi \approx -3.3 \text{ rad}$ (cf. Fig. 40) [42]. The finite hit density and the inefficiencies at the chamber boundaries account for 1/4 each. The single track efficiency is rather independent on the polar angle except when approaching the edge of the acceptance at low theta. At $\theta = 0.12 \text{ rad}$ the high momentum efficiency is dropping by 5% because of the finite hit density. Further work to improve the track efficiency at low momentum is still ongoing [11].

The momentum of a track is determined from the deflection in ϕ -direction. The deflection in θ -direction caused by a second order field effect is taken into account by applying a small correction. In addition to a two-parameter fit

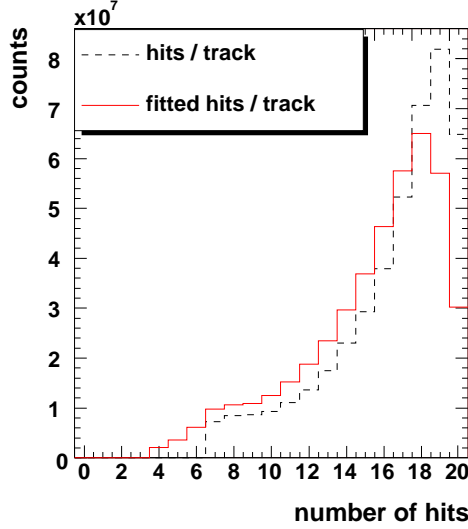


Fig. 38. Number of hits per track and fitted hits per track. On average one hit is excluded from the track fit due to its large residual. Tracks with less than 7 fitted hits are discarded.

in the ϕ - z plane, a three-parameter fit allows an azimuthal inclination of the track at the entrance of the TPC caused e.g. by prior multiple scattering. Fig. 41 shows the relative momentum resolution determined with a Monte Carlo simulation as a function of the momentum. The three-parameter fit yields an optimal result for low momentum tracks which often suffer multiple scattering. In contrast, high momentum tracks are better described by a two-parameter fit due to the additional vertex constraint. To exploit the positive aspect of both, a combined momentum

$$p_{comb} = \left(\frac{p_2}{\sigma_2^2} + \frac{p_3}{\sigma_3^2} \right) / \left(\frac{1}{\sigma_2^2} + \frac{1}{\sigma_3^2} \right), \quad (26)$$

is used, where p_2 and p_3 denote the two-parameter and three-parameter fits, respectively, and $\sigma_2 = \Delta p_2/p_2$ and $\sigma_3 = \Delta p_3/p_3$ are the corresponding resolutions. The relative momentum resolution of the TPC, which is determined by the resolution of the detector and multiple scattering, was determined by GEANT simulations and is given by:

$$\frac{\Delta p_{comb}}{p_{comb}} = \sqrt{(1\% \cdot p_{comb})^2 + (2\%)^2}, \quad (27)$$

with p_{comb} expressed in GeV/ c .

10.5 Calibration of hit positions

The hit reconstruction (cf. Sect. 10.1) is able to separate overlapping hits as long as their absolute maxima are at least one pixel apart. If this is not the case,

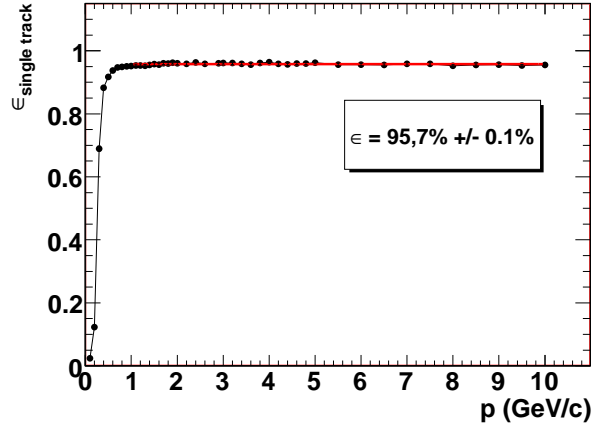


Fig. 39. Single track efficiency of the TPC as a function of momentum, obtained by embedding Monte Carlo tracks in experimental central Pb-Au events.

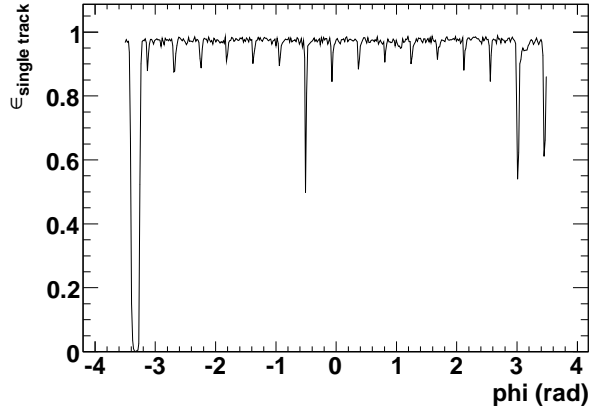


Fig. 40. The single track efficiency of the TPC as a function of azimuth.

the merged clusters are assigned to a single hit. These hits are recognizable by their unusually large cluster width of $\sigma_{cluster} > 0.6$ pad units (≈ 6.2 mm). A double or even triple peak structure becomes visible in the $\Delta\phi = \phi_{track} - \phi_{hit}$ distribution with increasing cluster width (Fig. 42) [28]. To correct for unrecognized overlapping hits the double peak structures were parametrized as a function of the distances d from the center and included as corrections in the track fitting procedure. The triple peak structures were neglected.

Further corrections of the hit positions in the TPC were obtained by using the additional information from other detectors. The tiny structures seen in the polar angle difference $\Delta\theta = \theta_{SDD,track} - \theta_{TPC,hit}$ between the SDD track segment and the TPC hits plotted vs. the pads of the TPC (Fig. 43, top) reflect the 16 readout chambers. No periodic structures were observed in the distribution of $\theta_{SDD,track}$. Using this knowledge the positions of the hits in the TPC were shifted by the amount $\Delta\theta_{cor}$ with respect to the mean value $\Delta\theta$ in each each chamber. The corrections were applied as a function of the polar angle θ to the individual pads and planes (Fig. 43, bottom).

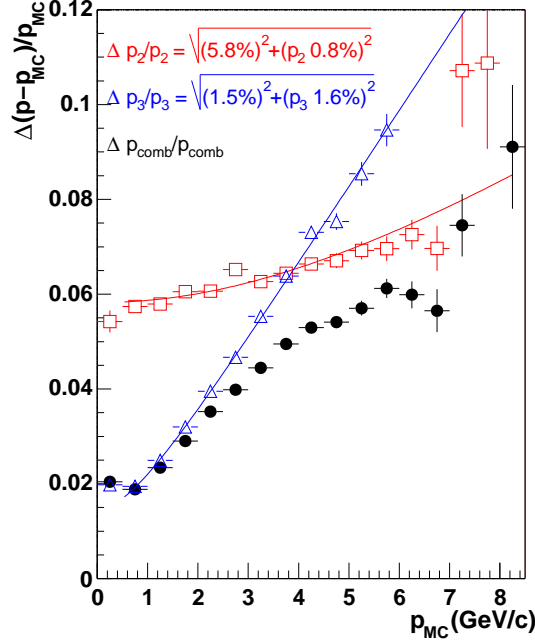


Fig. 41. Relative momentum resolution. The two-parameter fit (open squares) includes an additional vertex constraint and is optimal for high momentum tracks. The three-parameter fit (open triangles) allows an azimuthal inclination of the track at the entrance of the TPC and yields the best result for low momentum tracks which often suffer multiple scattering. The combined momentum fit (filled circles) combines the advantages of both.

A clean sample of high momentum pions ($p > 4.5$ GeV/c), selected with the RICH detectors, was used to study the azimuthal angle difference $\Delta\phi = \phi_{R2M} - \phi_{TPC,hit}$ between the TPC track segment as measured at the mirror of the RICH2 detector and the hits in the TPC (Fig. 44). The advantage of using a clean pion sample for calibration purposes is given by the similar multiplicities of π^+ and π^- differing by only 10% [43]. The deflection of oppositely charged particles with increasing plane number can clearly be seen in Fig. 44. With good approximation, the minima of the distributions are expected to be centered at zero because tracks with infinite momentum are not deflected (cf. Sect. 10.7). The deviations from zero were used to correct the hit positions of the TPC as a function of the azimuthal angle ϕ and the plane number. The same calibration was performed for the polar angle θ .

10.6 Hit position resolution

The result of the track fitting procedure can be improved by assigning individual weights to the hits according to their resolution. The weights contain the information about the hit positions in 3-dimensional space and about special hit characteristics. In this way remaining inaccuracies in the determination of the drift velocity are taken into account, as well as other dependencies like the hit amplitude or the hit multiplicity of the event.

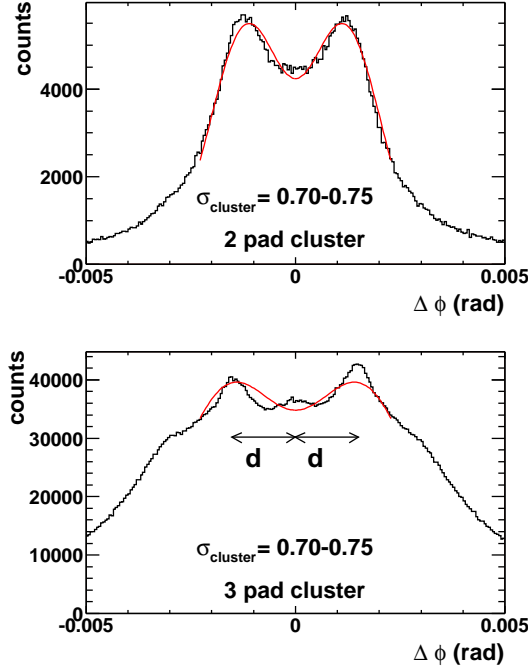


Fig. 42. The splitting of the $\Delta\phi = \phi_{track} - \phi_{hit}$ distribution in several peaks is due to unrecognized overlapping hits. The distance d of the peak to the center as a function of the cluster width is used to derive a correction for the hit position. The cluster width $\sigma_{cluster}$ is given in pad units.

As the momentum is determined from the deflection of a particle trajectory in the magnetic field, the azimuthal coordinate ϕ has a dominant influence on the momentum resolution. For this coordinate the hit position resolution $\Delta\phi$ was parametrized as a function of the radius, the 20 planes in the TPC, the hit amplitude, the hit multiplicity in the TPC, the number of responding pads, and the hit being isolated or not, and included as weights ($w = 1/\Delta\phi^2$) in the track fitting procedure.

Fig. 45 shows a subset of the 6-dimensional resolution matrices. For isolated hits, the 3 pad clusters have a somewhat better resolution than the 2 pad clusters due to the more favorable charge sharing. The resolution of overlapping hits deteriorates about a factor of two compared to isolated hits. Remarkable is also the strong dependence of the resolution on the amplitude. Firstly, the resolution improves with the amplitude. This effect can be ascribed to a better signal-to-noise ratio. Due to saturation effects the resolution deteriorates again at higher amplitudes. As expected, the resolution deteriorates with the number of hits in the TPC, though the effect is small. The linear improvement of the resolution with the radius has its origin in the increasing influence of the diffusion with the drift length. The dependence on the plane number of the TPC is due to the higher occupancy in the first planes, but also due to remaining uncertainties in the knowledge of the electric or magnetic field.

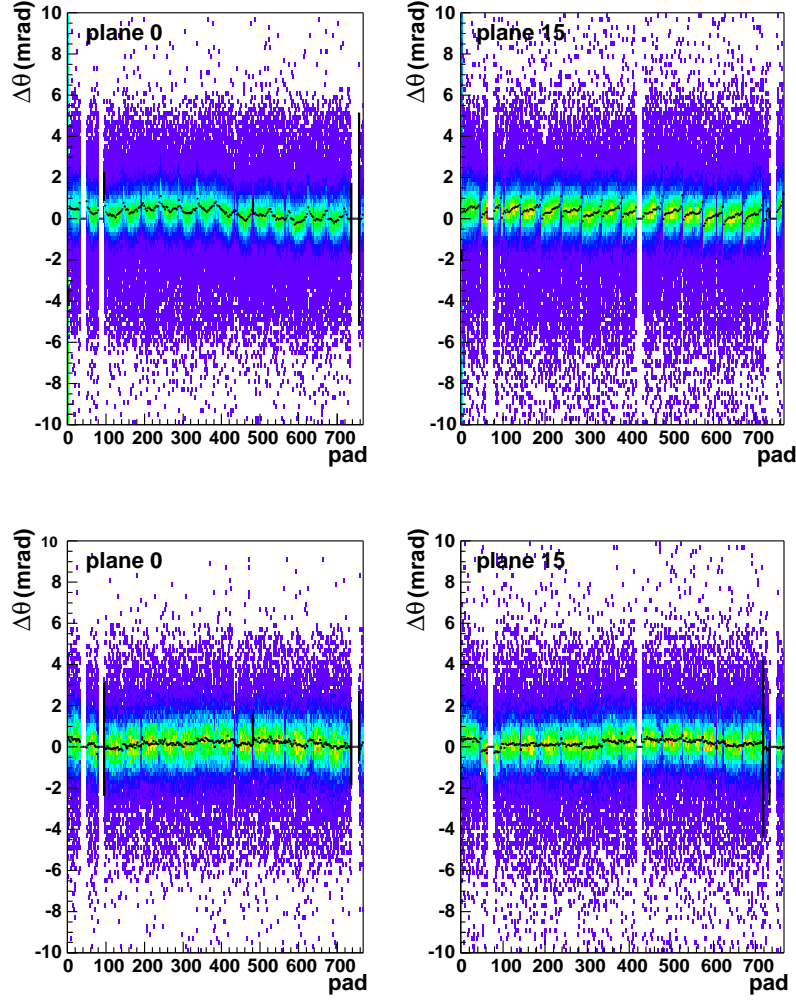


Fig. 43. Top: Polar angle difference $\Delta\theta = \theta_{SDD,track} - \theta_{TPC,hit}$ between the SDD track segment and the TPC hits plotted vs. the pads in the TPC. The black lines represent the bin-by-bin averages of the entries in the color scatter plots. The tiny structures reflect the 16 readout chambers of the TPC. Bottom: The same distribution after correction of the hit positions in the TPC.

10.7 Calibration of the momentum

The absolute measured value of a particle momentum can vary during the data taking period. It is caused by the fluctuation in the electric and the magnetic field, the change in the gas composition, temperature, and ambient pressure. The calibrations described in the previous sections removed most of these effects. The remaining variations are taken out phenomenologically by looking at the position of the minimum in the q/p -distribution (Fig. 46). Assuming similar abundances of positively and negatively charged particles and the infinite spatial and temporal resolution of the detector, the distribution of the charge over momentum (q/p) should have a minimum at zero (cf.

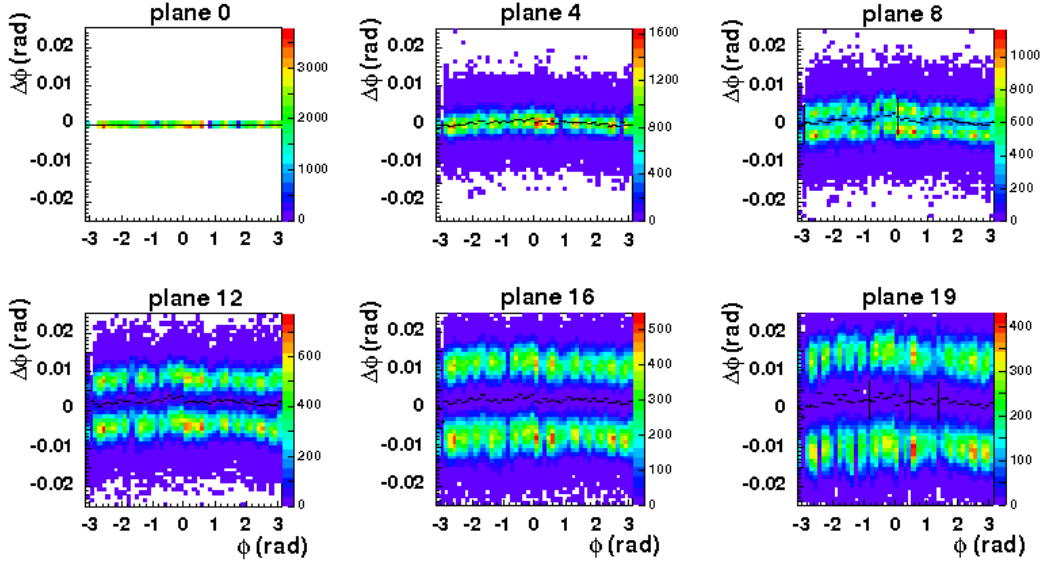


Fig. 44. Remaining apparent deflection for infinite momentum tracks. For a clean pion sample the azimuthal angle difference $\Delta\phi = \phi_{R2M} - \phi_{TPC,hit}$ is plotted vs. ϕ_{R2M} . The black lines represent the bin-by-bin averages of the entries in the color scatter plots. The valley between the positive and negative particles should, ideally, be at $\Delta\phi = 0$.

Sect.10.5).

The shift can be used to correct remaining deviations in the momentum. A convenient particle choice for this measurement is pions. As already discussed in Sect. 10.5 the multiplicities of π^+ and π^- are similar and effects related to a different abundance of particles with opposite charge are reduced.

To determine the proper position of the minimum with high accuracy, the reconstructed masses of Λ^- and $\bar{\Lambda}^-$ hyperons were compared as a function of momentum, while applying different shifts $\Delta(q/p)$. Only at the position of the proper minimum the reconstructed masses coincide.

For the calibration of the data a clean pion sample was selected with the RICH detectors by the ring radius. The determination of the shift of the minimum with respect to its proper position was performed in four steps in order to optimize statistics [44]. First, the data were divided in three groups:

- positive magnetic field at the beginning of the beam time,
- negative magnetic field, and
- positive magnetic field at the end of the beam time,

and a coarse correction was calculated as a function of the azimuthal and polar angle ϕ and θ . Second, a finer correction was derived in intervals of one hour data taking. The next calibration steps were performed on a pion sample identified via the differential energy loss dE/dx in the TPC. This allowed to increase significantly statistics, but decreasing the purity of the pion samples. The corrections were applied as a function of θ integrating over ϕ in finer

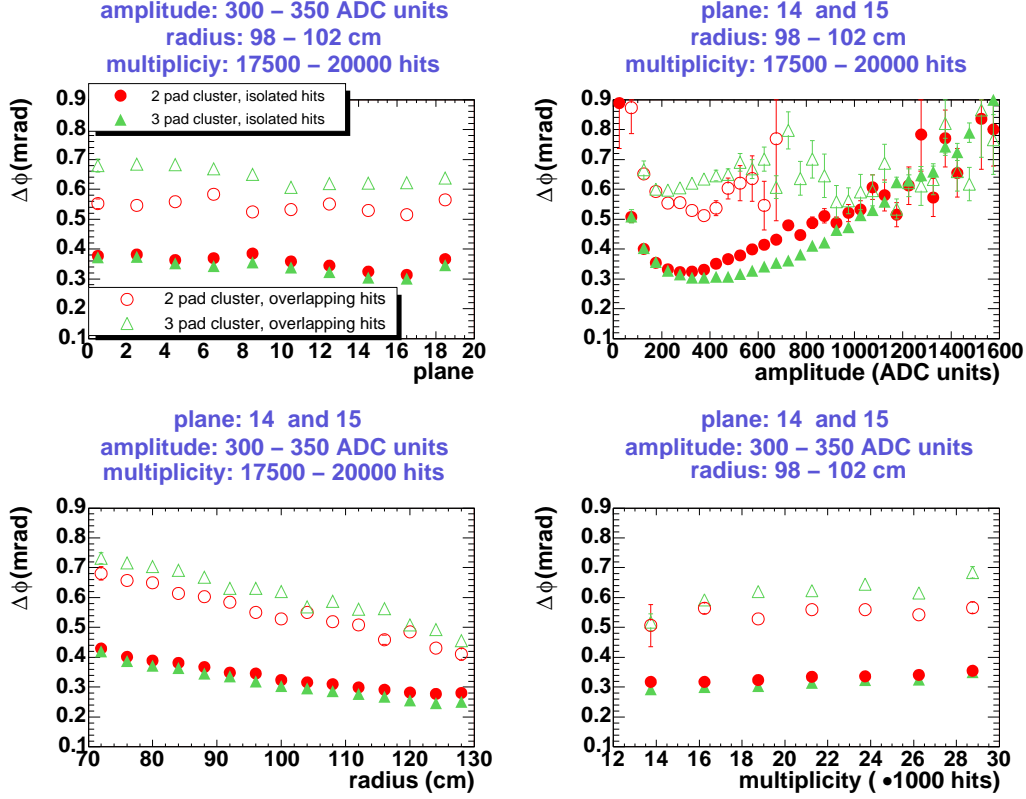


Fig. 45. The hit position resolution was parametrized as a function of the radius, plane, amplitude, hit multiplicity, number of responding pads and hit isolation status. This allowed to weight each hit individually in the track fitting procedure according to its characteristics.

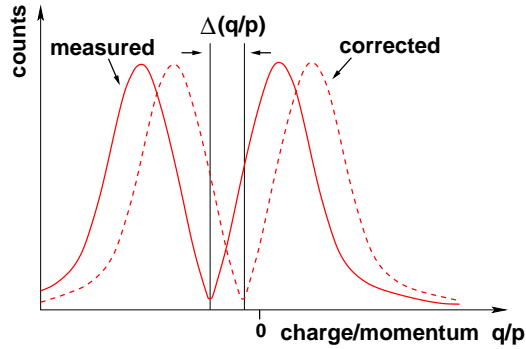


Fig. 46. A shift of inverse momentum distribution of positively and negatively charged particles can be used to determine the correction.

time scales. Finally, a last correction was determined in even finer entities of 10 bursts, but integrated over ϕ and θ . The effect of the momentum calibration on a pion sample selected via the dE/dx in the TPC can be seen in Fig. 47 where the minimum of the q/p -distribution is plotted as a function of time.

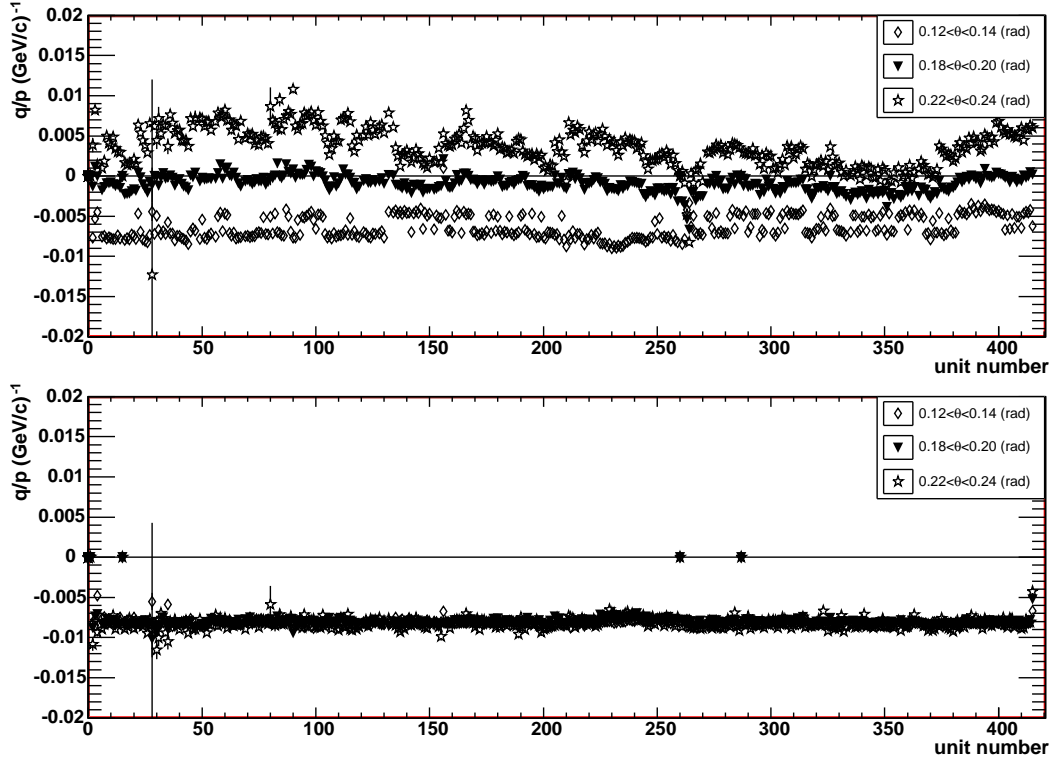


Fig. 47. Top: The minimum of the q/p -distribution plotted vs. calibration units (1 calibration units \approx 1 hour) for different polar angles θ without applying any momentum calibration. Bottom: After momentum calibration the position of the minimum remains stable.

10.8 Specific energy loss

The specific energy loss of charged particles at a given momentum carries information about the particle mass. In the CERES TPC the energy deposited along the track is sampled 20 times with each sample corresponding to a path length of approximately 2.4 cm (cf Fig. 20 in Sect. 7.4). The signal in each sample follows the Landau distribution with a long tail due to energetic delta electrons. The truncated-mean method, in which hits with lowest (one hit) and highest (40% of all hits) amplitudes are excluded, leads to a significantly improved dE/dx resolution. The truncated-mean energy loss measured in the CERES TPC for electrons, pions, kaons, protons, and deuterons is shown in Fig. 48.

After pad-to-pad calibration based on total amplitude in the pad of maximum amplitude (cf. Sect. 8.9), correction of undershoot after each pulse (cf. Sect. 8.7), and attachment correction taking into account different particle composition at different θ (cf. Sect. 6.7) the dE/dx resolution was improved from 18% [35] to less than 10% [10,35] for tracks with more than 15 hits. A comparison between the calibrated truncated mean dE/dx -resolution for electrons and the Allison/Cobb parametrization [45] is shown in Fig. 49 as a function of the number of hits per track. For the maximum number of hits the

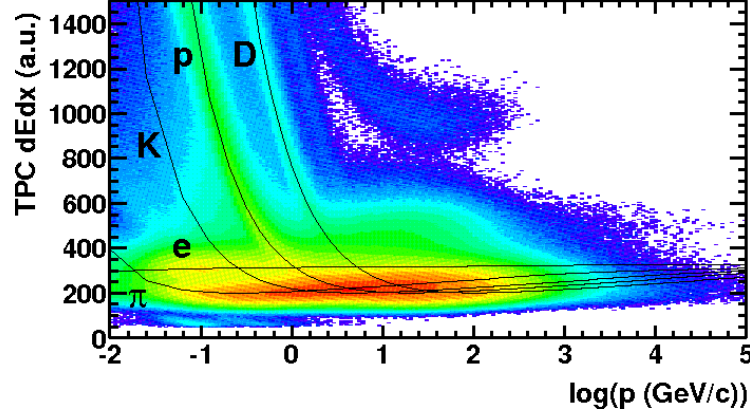


Fig. 48. The truncated-mean energy loss as a function of momentum for different particle species.

dE/dx -resolution approaches the parametrization. With the number of hits per track peaked at 18 (cf. Fig. 38) most of the electrons are measured with a dE/dx -resolution of better than 10%.

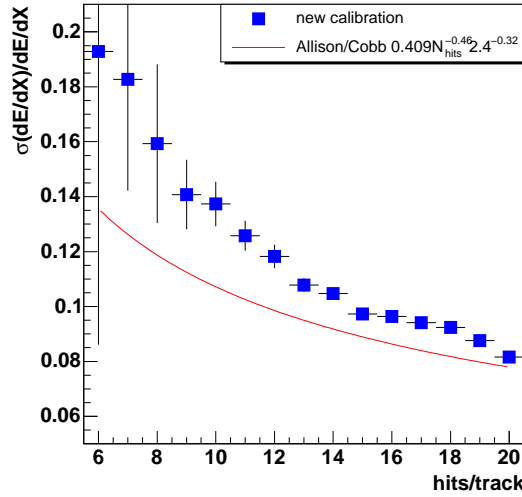


Fig. 49. Truncated mean dE/dx -resolution vs. number of hits per track (squares) compared with the parametrization by Allison and Cobb [45] (line). For a number of hits above 15 the dE/dx -resolution is better than 10%.

11 Performance of the TPC

For a track multiplicity between 350 and 400, the global position resolution achieved with the calibration of the TPC is $r\Delta\phi \approx 340 \mu\text{m}$ and $\Delta r \approx 640 \mu\text{m}$ [28] to be compared with the aimed design resolution of $r\Delta\phi^{design} = 250 - 350 \mu\text{m}$ and $\Delta r^{design} = 400 - 500 \mu\text{m}$ [6]. The design value was met for the azimuthal coordinate which has a crucial influence on the momentum resolution. Less effort was taken for the radial coordinate, where a detailed weight

determination for the individual hits (cf. Sect. 10.6) was disregarded. The improvements due to the complex calibration presented in this paper can be judged by comparing the position resolution with former values from a preliminary calibration, namely $r\Delta\phi \approx 500\,\mu\text{m}$ and $\Delta r \approx 800\,\mu\text{m}$ [25].

Fig. 50 shows the width of the residuals as a function of the plane number in the TPC. The azimuthal resolution varies between 0.4 mm at the point where the radial magnetic field is strongest and 0.3 mm close to the end of the TPC. The higher occupancy in the first TPC planes is responsible for the deterioration of the radial resolution. Furthermore, the drift length is on average longer in the first planes and thus diffusion plays a larger role.

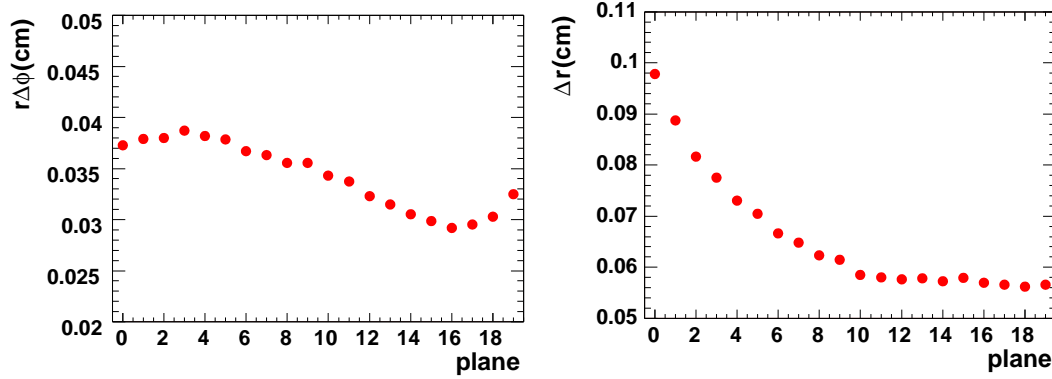


Fig. 50. Azimuthal (left) and radial (right) position resolution as a function of the plane number in the TPC.

Another informative quantity is the mass resolution of K_S^0 meson in the decay mode $\pi^+\pi^-$. The contribution of the pion masses to the mass of the K_S^0 is small. Thus, the mass resolution of the K_S^0 is sensitive to the momentum resolution. The calibration improved the width of the reconstructed K_S^0 mass from $22\,\text{MeV}/c^2$ [25] to $13\,\text{MeV}/c^2$ [28]. Furthermore, the performance of the TPC was confirmed in detailed Monte Carlo simulation over a wide range of parameters. Fig. 51 shows the agreement between the mass shift and width of the reconstructed K_S^0 meson in data and simulation over the whole range of transverse momentum. The mass shift indicates a bias in the momentum determination. However, the effect is small as compared to the average mass resolution of the K_S^0 of $13\,\text{MeV}/c^2$, indicating that the momentum bias is small as compared to the momentum resolution Δp .

The particle identification capability and the rejection power depends on the dE/dx -resolution. The pion rejection power of the TPC, given by the inverse of the pion misidentification rate, is shown in Fig. 52 as a function of the particle momentum for three different electron efficiencies [10]. For a particle momentum of $1\,\text{GeV}/c$ and an electron efficiency of 0.97 in the TPC (not shown in Fig. 52) the pion rejection power is 20 corresponding to a pion misidentification rate of 0.05. Combining the pion rejection power of the TPC and the two RICH detectors, the pion misidentification rate drops from $5 \cdot 10^{-4}$ (only RICH) to $2.5 \cdot 10^{-5}$ (RICH and TPC) at an electron efficiency of

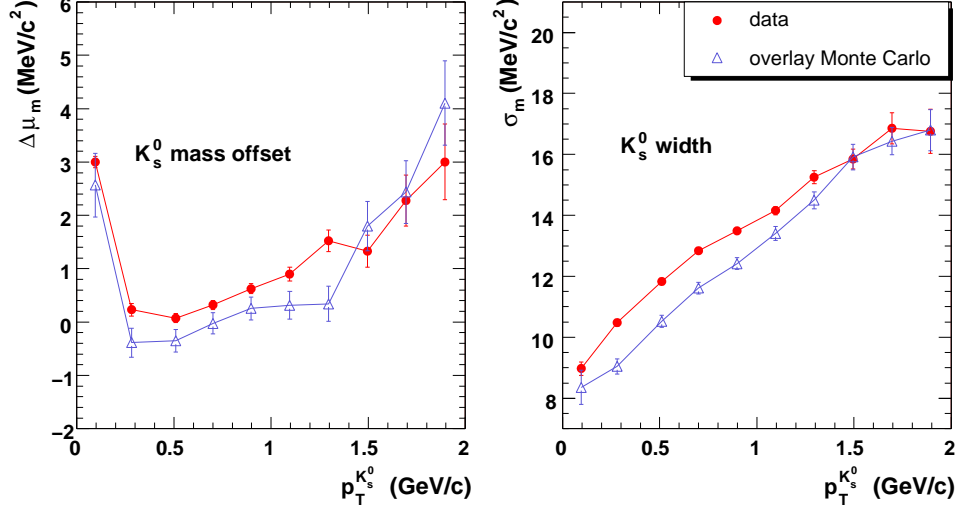


Fig. 51. Detailed simulations confirm the invariant mass shift (left) and width (right) of the K_s^0 meson over the whole range of transverse momentum. The points are connected by a line to guide the eye.

0.68 and 1 GeV/c particle momentum. This comparison corroborates the great improvements achieved due to the upgrade of the CERES spectrometer with the radial drift TPC.

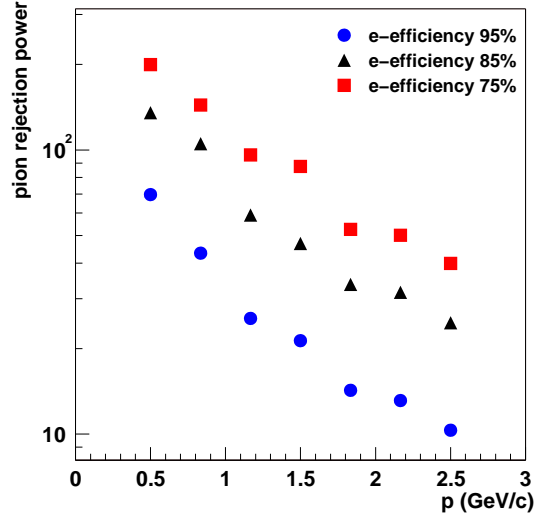


Fig. 52. Pion rejection power as a function of momentum for different electron track efficiencies.

12 Summary

The upgrade of the electron spectrometer CERES/NA45 with a radial drift TPC reached its objective to significantly improve the momentum resolution and the pion to electron separation capability. As a consequence, the study of lepton pair production in A-A collisions allowed for the first time to distinguish

between different theoretical approaches [10,12]. In addition, the TPC opened the possibility to access hadronic observables.

The CERES TPC is exceptional in terms of its radial electric field and inhomogeneous magnetic field configuration, both posing a great challenge to the calibration. The performance reached is close to the design specifications. With a spatial resolution of $340\text{ }\mu\text{m}$ in the azimuthal and $640\text{ }\mu\text{m}$ in radial direction, and with up to 20 space point measurements per particle track, a momentum resolution of $\Delta p/p = \sqrt{(1\% \cdot p)^2 + (2\%)^2}$ is obtained. This translates into a mass resolution of 3.8% ² for the ϕ -meson in the e^+e^- -decay channel.

In the course of calibration, on the other hand, the dE/dx -resolution of the TPC was brought down to the level of about 10% which allowed the experiment to significantly improve the electron/pion identification capability. With the help of the TPC, a pion rejection factor of 1:40000 at an electron efficiency of 0.68 was achieved for a particle momentum of 1 GeV/c.

13 Acknowledgment

We would like to thank Ettore Rosso, Wolfgang Klempt and their team for their advice during the design of the TPC. The help of Michel Bosteels and his team in constructing and taking into operation the gas system is gratefully acknowledged. Fabio Formenti was instrumental in planning the final readout scheme. We gratefully acknowledge the help of Bernd Panzer-Steindel and his team in the IT Division and we thank Anton Przybyla for the perpetual on-site support.

This work was supported by GSI Darmstadt, the German BMBF, the U.S. DoE, the Grant Agency and Ministry of Education of the Czech Republic, the Israeli Science Foundation, the Minerva Foundation, and the Nella and Leon Benoziyo Center for High Energy Physics Research.

References

- [1] G. Agakichiev et al., CERES Collaboration, Phys. Rev. Lett. 75 (1995) 1272.
- [2] G. Agakichiev et al., CERES and TAPS Collaboration, Eur. Phys. J. C 4 (1998) 231.
- [3] G. Agakichiev et al., CERES Collaboration, Phys. Lett. B 422 (1998) 405, nucl-ex/9712008.
- [4] D. Adamová et al., CERES Collaboration, Phys. Rev. Lett. 91 (2003) 042301, nucl-ex/0209024.

² The originally envisaged goal of about 2% [6] mass resolution was not achieved mainly due to multiple scattering in the mirror of RICH2 and elsewhere in the apparatus.

- [5] G. Agakichiev et al., CERES Collaboration, Eur. Phys. J. C 41 (2005) 475.
- [6] H. Appelshäuser, CERES Collaboration, Acta Physica Polonica B29 (1998) 3153.
- [7] A. Marín, CERES Collaboration, Nucl. Phys. A661 (1999) 673c.
- [8] A. Marín, CERES Collaboration, J. Phys. G30 (2004) 709, nucl-ex/0406007.
- [9] D. Miśkowiec, CERES Collaboration, Nucl. Phys. A774 (2006) 43, nucl-ex/0511010.
- [10] S. Yurevich, Doctoral Dissertation, University Heidelberg (2006).
- [11] O. Busch, Doctoral Dissertation, Technical University Darmstadt (2007).
- [12] D. Adamová et al., CERES Collaboration, nucl-ex/0611022 (2006).
- [13] CERES Collaboration, CERN SPSLC/96-35/P280/Add 1.
- [14] CERES Collaboration, CERN/SPSLC 96-50, SPSLC/R110.
- [15] <http://wwwinfo.cern.ch/ce/ae/Maxwell/Maxwell.html>.
- [16] R. F. Holsinger and C. Iselin, User Guide, CERN, Geneva 1984.
- [17] V. L. Highland, Nucl. Instr. Meth. 129 (1975) 497,
Nucl. Instr. Meth. 161 (1979) 171.
- [18] G. R. Lynch and O. I. Dahl, Nucl. Instr. Meth. B 58 (1991) 6.
- [19] S. Biaggi, Nucl. Instr. Meth. A421 (1999) 234.
- [20] <http://st-support-cooling-electronics.web.cern.ch>.
- [21] C. Markert, Diploma Thesis, University Frankfurt (1995).
- [22] DIVDIF (CERNLIB).
- [23] D. Vranic et al., ALICE TPC Technical Status Report, CERN/LHC 2000-001.
- [24] R. Veenhof, Nucl. Instr. Meth. A419 (1998) 726,
<http://garfield.web.cern.ch/garfield>.
- [25] W. Schmitz, Doctoral Dissertation, University Heidelberg (2001).
- [26] B. Yu. et al., IEEE Trans. Nucl. Sci. NS-38 (1991) 454.
- [27] E. Mathieson et al., Nucl. Instr. Meth. A234 (1984) 505,
Nucl. Instr. Meth. A279 (1988) 602,
Nucl. Instr. Meth. A277 (1989) 277.
- [28] W. Ludolphs, Doctoral Dissertation, University Heidelberg (2006).
- [29] R. Baur, G. Gramegna, and M. Richter, Nucl. Instr. Meth. A409 (1998) 278.
- [30] H. Tilsner, Doctoral Dissertation, University Heidelberg (2002).

- [31] J. Baechler et al., Proc. of the 4th Workshop on Electronics for LHC Experiments, Rome, 1998.
- [32] C. Engster et al., GSI Scientific Report (2000) 211.
- [33] L. Musa et al., Proc. of the IEEE Nuclear Science Symposium, Portland, 2003.
- [34] P. Ernst, Diploma Thesis, University Heidelberg (1997).
- [35] R. Renfordt et al., NA49 Collaboration, IKF-58, Ann. Rep. (1997) 4.
- [36] L. Dietrich, Diploma Thesis, University Heidelberg (2001).
- [37] F. Sauli, CERN 77-09 (1977).
- [38] D. Miśkowiec and P. Braun-Munzinger, next article in the same issue of NIM, arXiv:0801.4920.
- [39] W. H. Press, S. A. Teukolsky, W. T. Vetterling, B. P. Flannery, Numerical Recipes, Cambridge University Press (1992).
- [40] GEANT Manual, CERN, Geneva 1993.
- [41] F. Mosteller and W. Tukey, Data Analysis and Regression, Addison-Wesley (1987).
- [42] M. Kalisky, Doctoral Dissertation, Technical University Darmstadt, in prep.
- [43] A. Andronic, P. Braun-Munzinger, J. Stachel, Nucl. Phys. A772 (2006) 167, nucl-th/0511071.
- [44] D. Antończyk, Doctoral Dissertation, Technical University Darmstadt (2006).
- [45] W. Allison and J. Cobb, Ann. Rev. Nucl. Part. Sci. 30 (1980) 253.